Eidgenössische Technische Hochschule Zürich
Swiss Federal Institute of Technology Zurich

Tomographic Reconstruction of Dark States in Circuit Quantum Electrodynamcis

Master Thesis in Physics
Presented by Markus Oppliger
Supervised by Matthias Baur
Handed in to Prof. Dr. Andreas Wallraff
Labratory for Solid State Physics, ETH Zurich

Zurich, January 2, 2012

Abstract

This thesis studies quantum circuit electrodynamics, which is an implementation of cavity quantum electrodynamics with superconducting qubits as artificial atoms and a microwave resonator as a cavity. It is used to implement an effective Dicke-like model of two qubits and the Dicke states for one excitation are fully characterized. Also symmetry selective Rabi oscillations between the ground and the Dicke states are observed. For two and three qubit, the dispersive qubit-qubit coupling induces an avoided crossing. The qubit states of this anticrossing are characterized with quantum state tomography. Furthermore the entanglement generation, which is a truly quantum mechanical effect, of two and three qubits on a timescale of a few nanoseconds is studied.

Contents

Chapter 1

Introduction

In the early 19th century a revolution in physics was on its way. It would change the understanding of mankind, what light and matter is. This revolution would even change the perception of information. In the following introduction, this big revolution, its implication for information as well as its practical investigation will be outlined.

The triggers for the revolution were, among others, the photoelectric effect, the spectrum of the hydrogen atom, Brownian motion and the ultra violet catastrophe. They were all explained by quantizing matter or light. These early quantum mechanical approaches were often phenomenological and contradicting to each other [1]. They were summed up and extended by Erwin Schroedinger, Werner Heisenberg, Max Born and Wolfgang Pauli to form a consistent, revolutionary and fantastic theory of quantum mechanics. The concept of matter and light was completely altered, as both are simoultaneausly acting like waves and like particles in this theory. This is known as wave-particle duality.

Information encoded in these quantum mechanical states also changed the understanding of information. It is known as quantum information and differs from classical information to a large extent. When a quantum state is read out, it becomes the state associated with the measured value. An arbitrary state can not be cloned. And one of the most interesting difference is the entanglement of two quantum mechanical systems. Entanglement means, that the states are not correlated in a classical way. Nevertheless, the information which can be read out from a two level quantum system, the qubit, is equal to the information of one classical bit.

The big practical difference to the classical case is during information processing. This was investigated by David Deutsch with a universal quantum computer in 1985 [2]. He showed that it outperforms its classical counter part, the Turing machine, on certain tasks and it also allows for universal classical computation, as it can simulate the Turing machine. The two architectures are quiet similar, as a quantum computer operates with qubits, compared to bits. However the quantum computer can process many inputs in paralles, which is coming from the superposition principle [3].

Since this ground-breaking work many algorithms were found for the quantum computer. In 1994 Peter Shor came up with algorithms, which can factorize and take the logarithms of large numbers exponentially faster than a classical computer. This gathered a lot of attention, as it would be possible

to attack the commonly used "public-key" cryptography [4] successfully in a reasonable amount of time. Also the algorithm by Low Grover needs to be mentioned. It searches an unsorted data base quadratically faster than the classical algorithms[5].

Another very important application for quantum computers is the simulation of quantum systems. A classical computer can not simulate a quantum system with even a few degrees of freedom, as stated by Richard Feynman [6]. In the fields of nuclear physics, atomic physics and chemistry, many key system of interest, only have tens to hundreds of degrees freedom. Being able to simulate this quantum systems from first principle, could revolutionize many aspects of technology [7].

To implement a quantum computer, a physical system has to fulfill the DiVincenzo criteria [8]. They demand, that there are well-defined qubits, which can be intilized in a pure state and one needs to be able to apply an universal set of unitary transformation on the states. The state of each qubit needs to be individually measurable, as well as the coherence time of the system needs to be long, compared to the processing time.

Many practical approaches exist to implement such a quantum computer. A very promising architecture is the use of superconducting circuits. The qubits are based on Cooper Pair boxes. This qubits are coupled to each other by a superconducting transmission line, which also serves a readout. The interaction between the photons and the qubits is described by circuit quantum electrodynamics (QED).

This architecture is explored in the current thesis. The thesis is structured the following way: It starts with the theoretical background of circuit QED in Chapter 2. The experimental setup is discussed in the following Chapter 3. Chapter 4 is dedicated to fast control of the excited level of the qubit by means of magnetic flux pulses. The experimental results for two qubits are then presented in Chapter 5. It contains a discussion of Dicke states, dark states and fast entanglement protocols. This is followed by Chapter 6, talking about three qubit states and their anticrossing and the W-state.

Chapter 2

Theory review

One of the most promising practical implementation for quantum information processor is a circuit QED architecture. It realizes a cavity QED system by means of electrical circuits. Usually an LC-circuit serves as a 1D resonator which is coupled to another LC-circuit with a nonlinearity(artificial atom). The coupling between the two systems is impressively high in contrast to standard cavity QED experiments. The whole architecture gives relatively long coherence times (on the order of microseconds) with respect to the duration of the single universal gates. The resonator can be used for joint quantum non-demolition read-out [9] of the qubits and simultaneously as a coupling bus between them [10].

In order to understand this implementation, the theory of circuit QED and superconducting qubits will be shortly reviewed in this chapter. It starts with the architecture of the resonator and the quantization of the circuit in Section2.1. To study the superconducting circuit, which has an atom like energy spectrum, the evolution from the Josephson junction to the transmon qubit is outlined in Section 2.2. The building blocks are then combined to create a practical implementation of the Jaynes-Cummings Hamiltonian. This system is operated in far detuned regimes, which is addressed by Section 2.2.5

2.1 Microwave resonator

2.1.1 Coplanar waveguide

In our case, the resonator is implemented by a coplanar waveguide (CPW). The CPW is a practical implementation of the transmission line, which can be modeled as a series of lumped element circuits, see Fig. 2.1 b. Here C_l,L_l,R_l and G_l are the capacitance, inductance, resistance and conductance per unit length. The conductance G_l is normally related to loss in the dielectric whereas the resistance is coming from conduction loss[7]. The impedance of such a lumped element circuit is given by

$$Z_0 = \sqrt{\frac{R_l - i\omega L_l}{G_l - i\omega C_l}}. \tag{2.1}$$

The propagation coefficient γ for a wave $e^{\gamma l}$ propagating through the transmission line is given by $\gamma = \alpha + i\beta\sqrt{(R_l - i\omega L_l)/(G_l - i\omega C_l)}$, where α and β are

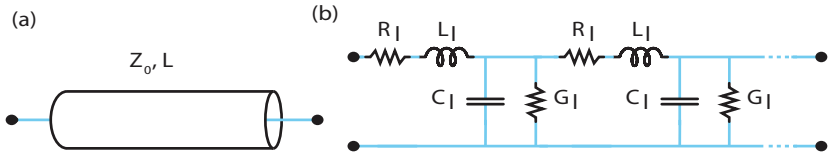

Figure 2.1: Transmission line: The transmission line can be modeled as infinite many single lumped element circuits. **a)** Representation of a transmission line as circuit diagram element. **b)** The single circuits have the same capacitance C_l per unit length and inductance L_l per unit length.

real coefficients. From this the attenuation, related to α, and phase evolution, related to β, of the wave can be extracted. This also defines the phase velocity $\nu = \omega/\beta$ at the frequency ω. In the lossless case the impedance becomes $Z_0 = \sqrt{L_l/C_l}$ and the wavelength of the wave is $\lambda = 2\pi/\beta = 2\pi\nu/\omega$

To build a resonator one can first introduce at a distance l a load impedance Z_L. The effective input impedance when looking into the transmission line at a distance l from the load impedance Z_L reads

$$Z_\mathrm{in} = Z_0 \frac{Z_\mathrm{L} + Z_0 \tanh \gamma l}{Z_0 + Z_\mathrm{L} \tanh \gamma l}. \tag{2.2}$$

When the transmission line is terminated with an circuit (infinite impedance), the input impedance becomes

$$Z_\mathrm{in}^\mathrm{open} = -Z_0 \coth \gamma l. \tag{2.3}$$

In a second step towards a resonator, one adds a second open impedance at the other end. Depending on the length one gets a high impedance(l=nλ/2) or a high admittance resonance(l=(2n+1)λ/4), where n is an arbitrary integer. In this thesis high impedance resonances have been used. The resonance frequency is then given by

$$\omega_\mathrm{in}^\mathrm{open} = \frac{1}{\sqrt{L_l C_l} \frac{n\pi}{l}}. \tag{2.4}$$

The resonator so far discussed could be capacitively coupled to a transmission line for interaction, with a capacitance C_k is introduced on both sides. Due to the large impedance mismatch the wave can be confined within the circuit. The impedance mismatch acts like a dielectric mirror in the Fabry-Perot cavity.

The loaded quality factor of the resonator is given by $1/Q_l = 1/Q_\mathrm{ext} + 1/Q_\mathrm{int}$ for the quality factor [11][12]. The internal quality factor $Q_\mathrm{int} \propto 1/\alpha$ is related to the dissipative energy loss. The external quality factor $Q_\mathrm{ext} \propto 1/C_\mathrm{k}$ is influenced by the input/output coupling. This can be engineered by the input capacitance and the real part of the load impedance. And the rate of energy loss κ is given by $\kappa = \omega/Q_\mathrm{L}$.

In our experiment the transmission line is implemented by a coplanar waveguide, depicted in Fig. 2.2. It resembles a 2D version of an coaxial cable: the ground is in the same plane as the center pin. An advantage of the CPW is that the gap can be scaled from microns to millimeters, thereby holding the

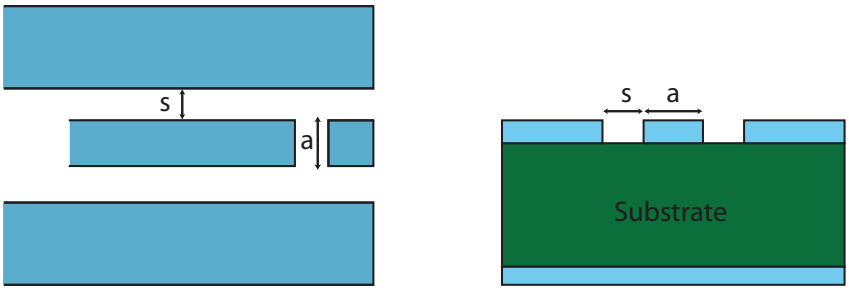

Figure 2.2: Coplanar-Waveguide. The center conductor is grounded and they can be seen as a 2 dimensional coaxial cable.

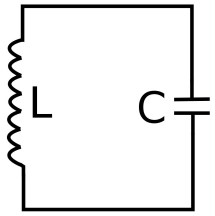

Figure 2.3: The LC-resonator is a non dissipative circuit with a inductance and a capacitance. It is the lumped element model of an electromagnetic resonator

same impedance Z_0[7]. The impedance Z_0 depends on the ratio of the center pin width a to the gap size s. Fig. 2.2. The central planes should be much larger than the gap size, in order approximate them as infinite. To receive the actual impedance of the coplanar waveguide, one can use conformal mapping [13]. And the resulting impedance is expressed with elliptical integrals.

The resonator build from coplanar wave guides can be seen as an analog to a one dimensional cavity. The role of a mirror for the photons is again played by two capacitance at both end. For one dimensional cavities the mode density gets reduces drastically. This is because the spatial expansion in the remaining 2 dimensions of 3 dimensional space is much smaller than the typical wavelength. This leads to enhancement of the electric field per photon of three orders of magnitude[12].

2.1.2 Circuit quantization

In the previous subsection, lumped element and distributed effective LC circuits were used to make an electronic harmonic oscillator. In this subsection, an LC circuit, seen in Fig. 2.3, will be described as a (quantum) harmonic oscillator, with the operators expressed in terms of electrical circuit quantities.

The equation of motion of the LC oscillator has the same form as the one for the harmonic oscillator [14, 15].

$$\frac{d^2Q}{dt^2} + \frac{Q}{LC} = 0, \tag{2.5}$$

where Q is the amount of charge on the capacitor. The quantization of such a circuit can be done in the same way, as for the harmonic oscillator. The commutation relation for the two conjugated variables charge $\hat{Q}$ and magnetic flux $\hat{\Phi}$ is the following $\left[\hat{Q}, \hat{\Phi}\right] = i\hbar$. Here the charge $\hat{Q}$ plays the role of the position coordinate, whereas the magnetic flux $\hat{\Phi}$ is the analog to the conjugate momentum. The Hamiltonian is $H = \hat{\Phi}^2/2L + \hat{Q}^2/2C$. In correspondence to the harmonic oscillator a creation $\hat{a^\dagger}$ and a annihilation $\hat{a}$ operator can be introduced and the Hamiltonian reads

$$H = \hbar\omega_0(\hat{a}^\dagger\hat{a} + {}^1/_2). \tag{2.6}$$

The resonance frequency is $\omega_0 = \sqrt{{}^1/_{LC}}$ and the commutation relation is $\left[\hat{a}, \hat{a}^\dagger\right] = 1$.

2.2 Superconducting Qubits

The spectrum of the circuits so far presented are harmonic. In order to be able to define a qubit, the spectrum needs to be anharmonic. To achieve this, one introduces another LC circuit with an anharmonicity, given by a Josephson junction. The Josephson junction is the only known dissipation free circuit element which is non linear [15].

2.2.1 Josephson junction

The Josephson junction consist of two superconducting electrodes separated by a thin isolating layer. The Josephson junction can be split into a pure Josephson element and a capacitor, see Fig. 2.4 a [16]. The Hamiltonian of this element is given by

$$\hat{H}_\mathrm{J} = -\frac{E_\mathrm{J}}{2}\sum_{n\in\mathbb{Z}}(|n\rangle\langle n+1| + |n+1\rangle\langle n|), \tag{2.7}$$

where $|n\rangle$ are the eigenstates of the charge operator $\hat{n}$ associated with the number of Cooper pairs on one side of the junction and E_J is the Josephson energy. One can see in this Hamiltonian the effect when a Cooper pair is tunneling through junction, denoted by $|n\rangle\langle n+1| + |n+1\rangle\langle n|$. Taking into account that the superconducting phase difference $\hat{\delta}$ and $\hat{n}$ are conjugate variables, the Hamiltonian takes the the form:

$$\hat{H}_\mathrm{J} = -E_\mathrm{J}\cos\hat{\delta}. \tag{2.8}$$

For the total Hamiltonian the contribution from C_J has to be taken into account as well. This is discussed in more detail in the next section.

2.2.2 Cooper pair box

The Cooper pair box consists of a Josephson junction, where one part is grounded, called reservoir and the other part is connected to a capacitor, called island. The capacitor can be biased by a gate voltage which, as seen in Fig. 2.4 b. There is now a second energy, the charging energy E_C, beside E_J. It is associated with

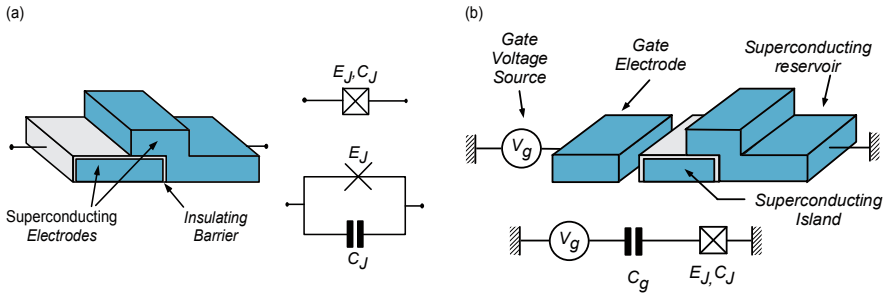

Figure 2.4: The Cooper pair box and the transmon a) Shows the Josephson junction and the corresponding circuit diagram b) The Cooper pair box is a Josephson junction which can be tuned over a gate capacitance [16].

the total capacitance of the Cooper Pair box. Accordingly the Hamiltonian reads

$$\hat{H} = E_{\mathrm{C}}(\hat{n} - n_g)^2 - E_{\mathrm{J}} \cos \hat{\delta}, \tag{2.9}$$

where $n_g = (C_{\mathrm{g}} V_{\mathrm{g}})/(2e)$ is the reduced gate charge and $E_{\mathrm{C}} = 2e^2/(C_{\mathrm{g}} + C_{\mathrm{J}})$. To solve the Schrödinger equation it is convenient to change to the phase representation. The equation is then a Mathieu equation [16]:

$$-E_{\mathrm{C}} \frac{\partial^2}{\partial \delta^2} \phi_k - E_{\mathrm{J}} \cos(\delta) \phi_k(\theta) = E_k \phi_k(\delta). \tag{2.10}$$

This equation can be solved analytically [17] by means of the Mathieu functions. The resulting energy bands are shown in Fig. 2.5. For $n_g \in 0.5\ \mathbb{Z}$, the energy degeneracy for the $E_{\mathrm{C}}(\hat{n} - n_{\mathrm{g}})^2$ energy is lifted by the Josephson term. This is in analog to the tight binding model. Also, at these points the linear charge noise is suppressed, because at this "sweet spot" the energy levels are to first order insensitive to the gate charge n_{g}. Cooper pair box based qubits are operated at $n_{\mathrm{g}} = 0.5$ with $E_{\mathrm{J}}/E_{\mathrm{C}}$ small. This gives a very good anharmonicity, meaning that $E_{01}/E_{12} \gg 1$, where E_{ij} is the energy gap between the ith and the jth level. Another fact to note is the flattening of the energy levels with increasing $E_{\mathrm{J}}/E_{\mathrm{C}}$ ratios. This regime is explored by state of the art transmon qubits.

In order to couple a drive to the qubit base on the Cooper pair box, one can introduce another interaction mechanism. This is done for example by coupling another voltage source V_{e} to the island. The resulting Hamiltonian is qualitatively the same as for the CPB in Equation (2.9). There is just a change in E_{C} and overall shift and n_{g} gets the additional term $n_{\mathrm{g}} - C_{\mathrm{e}} V_{\mathrm{e}}/2e$. If one works in the charge basis with only two states, the resulting Hamiltonian reads

$$\begin{aligned} \hat{H} &= \frac{E_{\mathrm{J}}}{2} \hat{\sigma}_z - \frac{E_{\mathrm{C}} C_{\mathrm{e}} V_{\mathrm{e}}}{2e} \hat{\sigma}_x \\ &= \frac{1}{2} \hbar \omega_q \hat{\sigma}_z + \hbar \Omega_x \hat{\sigma}_x. \end{aligned} \tag{2.11}$$

Where the $\hat{\sigma}_i$ are the Pauli operators and $\Omega_x = -\frac{E_{\mathrm{C}} C_{\mathrm{e}} V_{\mathrm{e}}}{\hbar 2e}$ is a Rabi frequency.

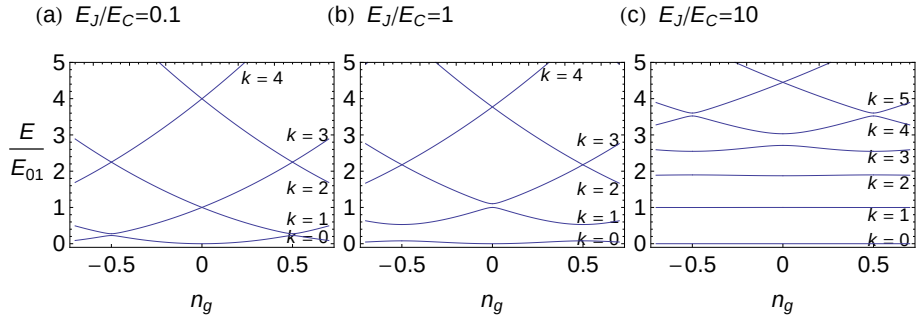

Figure 2.5: Energy Spectrum of the Cooper pair Box for different Coulomb and Josephson energy ratios. The energies are scaled by the energy between the ground and first excited energy level at $n_\mathrm{g} = 0$.

2.2.3 Split Cooper pair box

The split Cooper pair is a Cooper pair box, where the Josephson junction is split into two junctions, see Fig. 2.6[16]. They form a superconducting loop. The phase between the two superconducting parts can be changed by the magnetic flux Φ through the loop. For a loop with equal Josephson junctions, just the Josephson energy is shifted by

$$E_\mathrm{J} = 2E_\mathrm{J}^\mathrm{single} |\cos \pi \frac{\Phi}{\Phi_0}|, \tag{2.12}$$

where δ is the phase difference between the two superconductors. $E_\mathrm{J}^\mathrm{singleC}$ is the energy for a single Josephson junction, which was used in the previous Sections. $\Phi_0 = h/2e$ is the magnetic flux quantum, in which the Josephson energy is periodic. The energy spectrum stays qualitatively the same as for the Cooper pair box, but the Josephson energy is tunable. If the junctions are not equal E_J acquires additional terms.

2.2.4 Transmon

For a long time the $E_\mathrm{J} \ll E_\mathrm{C}$ regime was not explored for qubit production, as the anharmonicity was not high enough. This is not the case for the transmon qubit. With its design, the qubit anharmonicity decreases with a low power law in $E_\mathrm{J}/E_\mathrm{C}$, while the charge dispersion reduces exponentially with $E_\mathrm{J}/E_\mathrm{C}$[18]. This is achieved by introducing an extra capacitance C_B between the superconducting island and the reservoir and a similar scaling of the gate capacitance C_g, see Fig. 2.7. It doesn't need to be operated at the charge "sweet spot", because the charge dispersion is very flat and the qubit is therefore insensitive to charge noise. The effective Hamiltonian stays the same as for the split CPB.

If one now couples this qubit to a model of the transmission line resonator, one gets the following effective Hamiltonian [18]

$$\hat{H} = 4E_\mathrm{C}(\hat{n} - n_\mathrm{g})^2 - E_\mathrm{J} \cos\delta + \hbar\omega_\mathrm{r}\hat{a}^\dagger\hat{a} + 2\beta e V_\mathrm{rms}^0 \hat{n}(\hat{a} + \hat{a}^\dagger). \tag{2.13}$$

Here $\hat{a}, \hat{a}^\dagger$ denotes the annihilation-/creation operator, $\omega_\mathrm{r}^2 = 1/L_\mathrm{r}C_\mathrm{r}$ is the local oscillator frequency and $V_\mathrm{rms}^0 = \sqrt{\hbar\omega_\mathrm{r}/2C_\mathrm{r}}$ is the root mean square voltage of

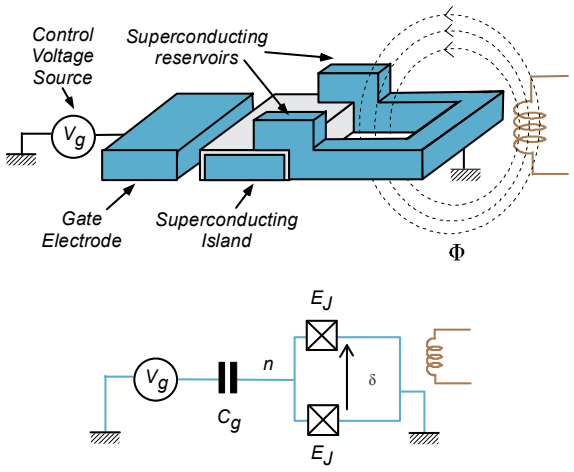

Figure 2.6: The split Cooper pair box can be biased using an external magnetic flux source [16].

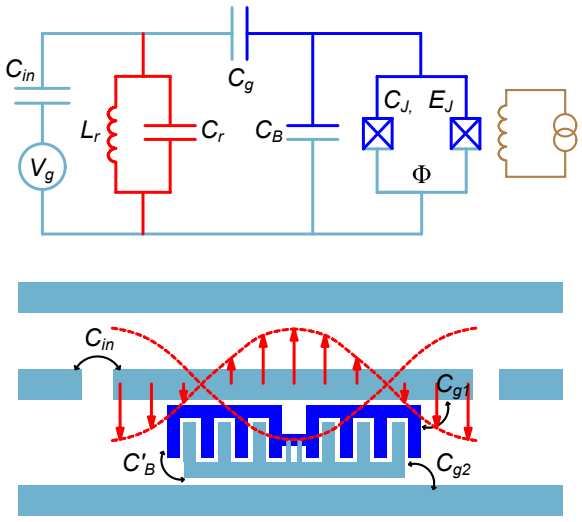

Figure 2.7: Transmon Qubit coupled to a transmission line, a) schematic drawing of the implementation of b). The Transmon qubit is seen on the right hand side. It can be biased by external coils (brown) ant it is coupled to a transmission line (red/blue)

the resonator and β is the ratio between the gate capacitance C_g and the total capacitance $C_\Sigma = C_\mathrm{B} + C_\mathrm{g} + C_\mathrm{J}$. The charging energy is given by $E_\mathrm{C} = e^2/2C_\Sigma$. The j^{th} energy level of the transmon can be found from the first two terms in the Hamiltonian (2.13). When the terms are approximated in $E_\mathrm{C}/E_\mathrm{J} \ll 1$ up to 4^{th} order the energy is given by [18]

$$\hbar\omega_j = -E_\mathrm{J} + \sqrt{8E_\mathrm{C}E_\mathrm{J}}(j + \frac{1}{2}) - \frac{E_\mathrm{C}}{12}(6j^2 + j + 3). \tag{2.14}$$

Equation 2.13 forms a generalized Jaynes Cummings Hamiltonian for the bare Transmon states [18],

$$\hat{H} = \hbar\sum_j \omega_j |j\rangle\langle j| + \hbar\omega_\mathrm{r}\hat{a}^\dagger\hat{a} + \hbar\sum_{i,j} g_{ij}|i\rangle\langle j|(\hat{a} + \hat{a}^\dagger), \tag{2.15}$$

with the coupling strength $g_{ij} = 2\beta e V^0_\mathrm{rms}\langle i|\hat{n}|j\rangle$. When approximating the transmon perturbatively, applying the rotating wave approximation and examining off-diagonal matrix elements, this Hamiltonian can even be reduced further[18]. The result is a block diagonal Jaynes Cummings Hamiltonian with only nearest neighbor coupling $g_{i,i+1}$.

$$\begin{aligned}\hat{H} = \hbar\sum_j \omega_j |j\rangle\langle j| + \hbar\omega_\mathrm{r}\hat{a}^\dagger\hat{a} \\ + \hbar(\sum_i g_{i,i+1}|i\rangle\langle i+1|\hat{a}^\dagger + H.c.)\end{aligned} \tag{2.16}$$

Here *H.c.* stands for the Hermitian conjugate. This Hamiltonian conserves number of excitations, meaning that it commutes with the operator $N_\mathrm{exi} = \hat{a}^\dagger\hat{a} + \sum_j \omega_j|j\rangle\langle j|$ [19]. This is very convenient, as to diagonalize this Hamiltonian, only states with the same number of excitations have to be taken into account.

2.2.5 Dispersive limit

The dispersive limit of the Jaynes Cummings Hamiltonian is highly interesting, since it allows a Quantum-Non-Demolition(QND) readout of the qubit. Another remarkable application is the coupling between different qubits via virtual photons. The dispersive limit is the regime where the detunings $\Delta_i = \omega_{i,i+1} - \omega_\mathrm{r}$ between the resonator and the qubit is large, in particular $g_{01}/|\Delta_i| \ll 1$, $g_{01}/|\Delta_i + \alpha| \ll 1$ for all levels, where $\alpha = \omega_{12} - \omega_{01}$ is the anharmonicity. The Hamiltonian (2.16) can then be transformed by using a canonical transformation and the Hausdorff relation to a two level Hamiltonian[18]

$$\hat{H}_\mathrm{eff} = \frac{\hbar}{2}\omega'_{01}\hat{\sigma}z + \hbar(\omega'_\mathrm{r} + \tilde{\chi}\hat{\sigma}_z)\hat{a}^\dagger\hat{a}. \tag{2.17}$$

Here $\omega'_{01} = \omega_{01} + g/01/\Delta_0$ is the Lamb shifted transition frequency of the qubit, $\omega'_r = \omega_\mathrm{r} - g_{12}/(2\Delta_1)$ is renormalized resonance frequency of the resonator. The dispersive shifts are given for the transmon limit as

$$\tilde{\chi} \approx -g^2_{01}\frac{E_\mathrm{C}/\hbar}{\Delta_0(\Delta_0 - E_\mathrm{C}/\hbar)}. \tag{2.18}$$

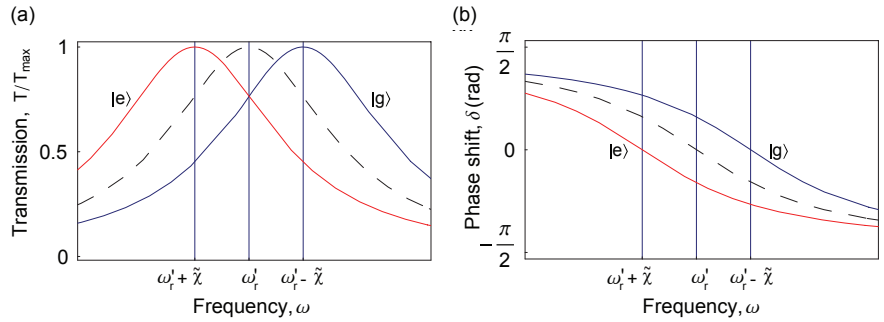

Figure 2.8: Qubit state dependent transmission spectrum a) transmission amplitude, which depends on the state of the qubit: it is plotted with for a resonator with an excited (red) qubit and a qubit in the ground state(blue), as well as for the resonator without a qubit at all (dotted) b) relative phase shift of the transmitted microwave [12]

The $\tilde{\chi}$ term accounts for the presence of the transmon in the resonator. It shifts the resonance frequency depending on state of the qubit. This can be used to perform Quantum-Non-Demolition measurements of the qubit state. This class of measurement is very interesting, as it leaves the measured state unchanged and can therefore be repeated many times. In the current work, it was used to read out the qubits in a time resolved measurement.

This was done by applying a continuous coherent measurement tone with the amplitude $\epsilon_{\mathrm{m}}(t)$ and the frequency ω_{m} to the resonator[20], which can be described by

$$\hat{H}_{\mathrm{drive}} = \hbar\epsilon_{\mathrm{m}}(t)(e^{-i\omega_{\mathrm{m}}t}\hat{a}^{\dagger} + H.c), \tag{2.19}$$

As seen from Equation (2.17) the resonator frequency incorporates information about the qubit state. Hence by measuring the shift of the resonator, the state of the transmon can be deduced.

It is done by observing the transmitted signal at a fix frequency. Normally it is chosen to coincide with the resonator frequency $\omega_{\mathrm{r}}' - \tilde{\chi}$ for the qubit in the ground state. As seen from Fig. 2.8 a and b, the transmitted amplitude as well as the phase shift of the signal can be used. In our case, one quadrature of the heterodyne detected signal was measured. This scheme can also be used to read out higher excited transmon levels and as a simultaneous read-out of multiple qubits coupled to the resonator. Even single shot readout for up to 3 qubits have been demonstrated [21, 22, 12].

Chapter 3

Measurement Setup

The conducted experiments were all in the gigahertz/megahertz regime. The wavelengths are on the scale: 1mm - 1m. For these wavelengths, the main technology development has been done for telecommunication and radio-astronomy. However, as the aim is to study coherent physical phenomenas with single energy quanta, very low powers, down to 10^{-18} W, need to be detected. Beside this challenge, another key aspect of the experimental setup is the thermal isolation of the system to avoid distortion of the quantum mechanical system, which destroys the coherence.

The components to achieve this goals as well and to perform the experiments are discussed in this chapter. It starts with the fabrication of the sample in Section 3.1 and proceeds with the cryogenic setup in Sections 3.2 and 3.3. The attenuation/amplification (Section 3.4) generation (Section 3.5) and detection(Section 3.6) of microwave signals are discussed thereafter.

3.1 Sample

Various methods are used to fabricate the sample. Standard photo-lithographic processes had been employed for the coplanar waveguide. They are made out of Niobium which turns superconducting at liquid Helium temperatures. It is sputtered on a sapphire substrate and then patterned with reactive-ion etching techniques. To get a specific resonator frequency, witch depends on the length of the resonator, a meander form had been applied. Here the curvature needed to be lower than the distance between the coplanar waveguides centerpin.

The transmons are made out of Aluminum, using standard electron beam lithography. A double angle shadow evaporation technique is used to deposit two Al layers. This step includes an oxidation to form the Josephson junctions. The charging energies E_{C}, the Josephson energy E_{J} and the coupling g of the transmon to the resonator can be engineered independently. The resulting chip is shown in Fig. 3.1

In this sample there were 3 transmon qubits with charging energies $E_{\mathrm{C}}/h =$ (0.264, 0.296, 0.307) GHz, maximum qubit transition frequencies $\nu_{A,B,C}^{\max} =$ (6.714, 6.050, 4.999) GHz and the coupling strength to the resonator $g/2\pi =$ (0.36, 0.30, 0.34) GHz. At the maximal frequencies the energy relaxation time is $T_1 =$ (0.55, 0.70, 1.10)μs and the phase coherence time $T_2^\star =$ (0.45, 0.60,

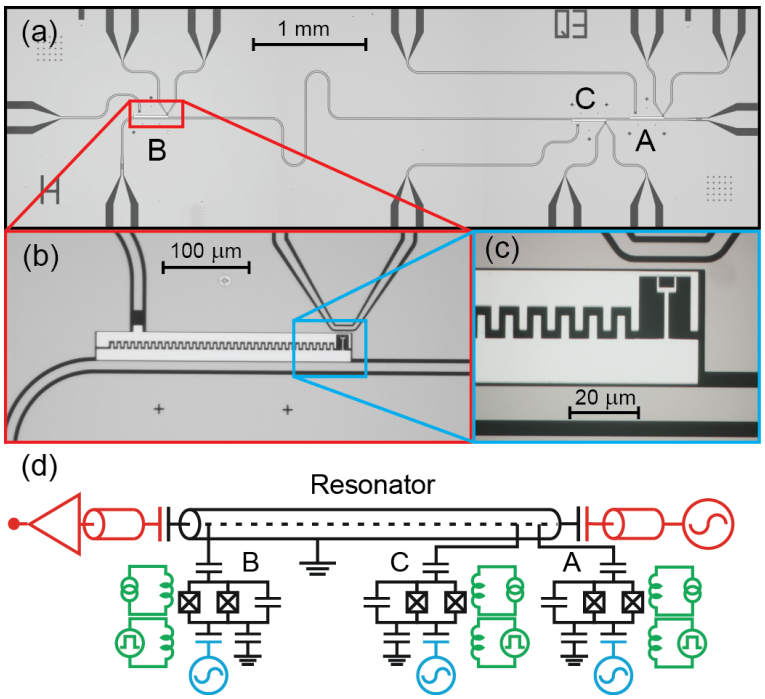

Figure 3.1: Optical microscope image of the chip a) The Transmon qubits A,B and C are at the end of the transmission line resonator. b) The Transmon qubit with its large capacitance C_B and the charge line on the left and the flux line on the right c) Zoom to the Josephson junctions, which can be seen on the upper right of the picture d) lumped circuit diagram of the chip: The black parts are the resonator and the transmons, the green elements are the coils resp. the flux lines and the blue ones are the charge lines for fast qubit manipulations.

0.65)μs. The resonator has a bare frequency of $\nu_r = 8.625$ GHz and a quality factor of Q = 3300 [23, 24].

3.2 Wiring, electromagnetic shielding and coils

To connect microwave cables to on-chip transmission lines, used for qubit manipulation and readout, the chip was placed on a printed circuit board (PCB). Here, the main challenge is the elimination of parasitic resonances caused by impedance mismatches. This PCB is placed in a copper sample holder, in order to shield the chip from electromagnetic fields. Again the suppression of unwanted resonances is the main design goal for the holder. The sample holder is connected with semi rigid coaxial cables. For biasing the three transmons, three superconducting coils where are placed beneath the sample.

3.3 Cryogenic setup

The typical energy scale of a transmon is 1-10 GHz, which is in the order of 50-500 mK. The big challenge is to minimize the temperature and its fluctuation as well as the Josephson noise. On the other hand, the signals which carry the readout and manipulation pulses need to be distorted as little as possible by the cryogenic setup. This is in order to keep a good signal to noise ratio.

To get the temperature as low as possible the dilution refrigerator Kelvinox 400HA from Oxford was used. Dilution refrigerators use the fact that below 870 mK a ^{3}He and ^{4}He mixture splits into a ^{3}He rich and a ^{3}He poor phase. For ^{3}He it takes energy to cross the phase boundary from the rich to the poor phase. By pumping on the poor phase, ^{3}He is moving from the rich to the poor phase. This means taking ^{3}He away from the poor phase. To restore equilibrium, ^{3}He is crossing the phase boundary. This takes energy and therefore effectively cools the system. In order to be in a continuous mode, the ^{3}He is again fed into the system on the ^{3}He rich phase. Like this temperatures down to 5 mK are reachable.

3.4 Microwave attenuation/amplification

Microwaves are generated at quite high powers of -30dBm to 15 dBm, but just -145 dBm are needed at the input of the chip for measurement and -60dBm for single qubit gates in the nanosecond regime[12]. The specific numbers depend on the capacitive coupling strength between the relevant transmission line.

For the radiation above 100mK, the Johnson noise, generated by the thermal agitation of charge carriers in the conductor, is the dominant noise source for microwave radiation. The noise power spectral density scales linearly with the temperature T and the resistance R as $S_{\bar{V^2}} = 4k_BT$ and k_B is the Boltzmann constant. As just a very small fraction of the generated signal is needed, the easiest way to get rid of the thermal radiation, is to attenuate the signal at low temperatures [12]. So to get the same signal to noise ratio at 300 K and 4 K one has to attenuate the signal by 20 dB. This is no problem, as the cooling power of the refrigerator is roughly 23dBm at the 1.5K stage. Therefore the signal is sequentially attenuated at different temperatures.

On the other hand, when the signal is leaving the cavity, it has very low power - roughly one photon energy per cavity photon lifetime. In order to detect this signal, one needs to amplify the signal. The amplification is done by a chain of high electron mobility transistor (HEMT) amplifier. The noise temperature of this array can by be calculated using Fri's law. In order to prevent the photons going back from the first amplifier to the sample, circulators were used.

3.5 Microwave generation

The microwaves for qubit manipulation and readout are generated using microwave generators E8257D from Agilent, which produce a phase coherent continuous wave. To modulate the phase and the amplitude of the signal on a nanosecond timescale, arbitrary waveform generators (AWG) 5014 from Tektronix and mixers from Marki are used. These mixers have a local oscillator (LO) input, two intermediate frequency (IF) input and a radio frequency (RF) output. They have typical frequencies of DC-500 MHz for the IF and GHz for RF and LO ports. In the mixer the LO is split into 2 parts. One is phase shifted by 90 degrees and the other is not modified. The first part gets multiplied by one of the IF inputs, the so called Q quadrature and the second part gets multiplied by the other IF input, the I quadrature.

The resulting output signal has generally 2 different frequencies, called sidebands, $\nu_{\mathrm{LO}} - \nu_{\mathrm{IF}}$ and $\nu_{\mathrm{LO}} + \nu_{\mathrm{IF}}$, where ν_{LO} and ν_{IF} denotes the frequencies of the corresponding input signals. The output frequencies as well as the phase of the signal can be selected. For example, if the I and the Q quadrature have a phase shift of $\phi = \pm\pi/2$ and have the same amplitude, only the left sideband/ right sideband doesn't vanish and the RF amplitude is proportional to the IF amplitude.

Leakage of the LO signal or of signals at the other sideband frequency can cause a major problem for accurate state preparation. This leakage is driving the qubit although it should be switched off. It can be reduced by pulsing the LO or by using an IF frequency around 100 MHz, so that the LO leakage is far detuned from the used sideband. In addition one can accurately calibrate the phase ϕ, I and Q offsets to reduce unwanted leakage signals.

3.6 Microwave detection

For data acquisition a PCI card from Acquiris is used. This card has an on board analog to digital (AD) converter. The sampling rate of the card is one Giga-Samples per second (1 GS/s). In order to fully analyze the signal, it is down converted by mixing it with a coherent tone before detection. The heterodyne detection scheme is done by applying an LO frequency offset by $\nu_{\mathrm{IF}} = 20$ MHz. The I and Q quadratures were processed further: They are low pass filtered in order to eliminate high frequency noise. As mentioned in Section 3.4, the signal to noise ratio is bellow 1. Therefore the coherently mixed signal is averaged in order to remove the uncorrelated noise.

Chapter 4

Flux Pulses

In the experiments carried out during this in thesis, it it crucial to tune the qubit frequency on a fast nanosecond time scale. This is achieved with short current pulses sent through a transmission line passing by the the SQUID loop of the qubit. These current pulses change the magnetic flux Φ through the loop. For the generation of the current pulses, an AWG from Tectronix is used. The experiments, discussed later in Section 5, require a high precision of the current pulses, they need to be accurate up to the mil. But there are many factors who modify the signal. Even the AWG itself, on the coaxial cables from the AWG to the refrigerator, on the cables down to the sample and the circuitry on the chip itself introduces distortion. To tackle this problems an introduction to classical control theory and the correction schemes will be given in Section 4.1. The results from examining the magnetic flux pulses will be shown in Section 4.2.

4.1 Classical signal theory

The aim of this Section is to explain how to get a desired output signal from a linear system. The output y(t) for such a system is given by

$$y(t) = \int_{-\infty}^{\infty} d\tau x(\tau) g(t-\tau). \tag{4.1}$$

Here x(t) is the input function and g(t) is the impulse response function. It is the response of the system to a delta-distribution, so an infinity high and infinity short, input signal. In the ideal case it should also be an delta-distribution and the signal gets transmitted without modification. Normally the response function is not known and needs to be measured. It is highly depending on the physical system. This function depends highly on the physical systems. To investigate this function, one can rewrite Equation (4.1) in the Fourier space. It simplifies due to convolution theorem to

$$Y(\nu) = X(\nu)G(\nu), \tag{4.2}$$

where $G(\nu)$ is the transfer function and capital letters stand for the Fourier transform of the corresponding quantity. The transfer function can be seen as filter of the original signal.

In the ideal case, the easiest way to find the impulse function is to apply a Dirac delta-distribution as an input in the time domain. The output y(t) is then the impulse response g(t), what can be seen from Equation (4.1). This strategy is applied in our experiment in the discrete way, by replacing the delta-distribution by the Kronecker delta.

Another approach to tackle the problem is to apply a Heaviside step function as an input. Only the rise, instead of the rise and the fall at the same time, of the pulse are examined. The output is given by

$$y(t) = \int_0^\infty d\tau g(t-\tau) \tag{4.3}$$

and $g(t) = \dot{y}(t)$. Now we want to correct for g(t), in order to choose the output signal. To do so, one can work in a discrete or in a continuous representation. In the continous limit and for a infinite long measurement time they are equal. First we want to have a look at the continous approach, where the analysis is simpler. Then we move on to the discrete representation, which is more suited for data processing.

In the Fourier space of the continous representation, the correction is simply given by $C(\nu) = 1/G(\nu)$, as seen from Equation (4.2). Due to the associativity of the convolution one gets the desired output:

$$y(t) = g(t) \star (c(t) \star x(t)) = x(t) \tag{4.4}$$

If the Fourier transform $G(\nu)$ is zero for a certain frequency ν, the correction has a singularity and the method breaks down. This is not the case for many applications.

Knowing the response function, one can generate any output signal. In practice this is limited by the restricted sampling frequency and channel filtering. As the data processing is discrete in our experiments, the analysis is done in a discrete manner. So integrals become sums and the Fourier Transform becomes a discrete Fourier Transform (DFT). In analog to Equation (4.1), the output signal is then given by

$$\vec{y} = g\vec{x}, \tag{4.5}$$

with $y_j = y(jT_\mathrm{c})$ and $x_i = x(iT_\mathrm{s})$. $\tilde{G}c_{ij} = g(jT_\mathrm{c} - iT_\mathrm{s})$ is the convolution matrix, T_s is the sampling rate of the AWG and T_c is the sampling rate for the convolution. T_s is constrained by the AWG, whereas T_c can be chosen arbitrarily. In order to get signal as continous as possible and to make $\tilde{G}_{ij}$ periodical, T_c is set to $T_\mathrm{s} = 10T_\mathrm{c}$. So, if one is interested in a pulse of length T, $\tilde{G}$ is a $\{T/T_\mathrm{s}, T/T_\mathrm{c}\}$ matrix.

In order to find a $\vec{x}$ for an optimal $\vec{y}$, as close as possible to the desired $\vec{y}^\star$, one can minimize the error $\|\vec{y}^\star - \tilde{G}\vec{x}\|$ in a dedicated norm. For the 2 norm this gives a least square approximation. This problem is solved by the pseudoinverse

$$L = (\tilde{G}^T\tilde{G})^{-1}\tilde{G}^T. \tag{4.6}$$

4.2 Flux pulse measured

The presented methods in Section 4 for flux pulse correction are experimentally easy at room temperatures. Measuring the actual signal seen by the qubit is

more demanding, because it can not simply be measured with a commercial high frequency oscilloscope. Instead we use the qubit itself as flux pulse "spectrometer" [25] [1]. The applied pattern can be found in Fig. 4.1. During the flux pulse a microwave, with constant length and amplitude, is applied to the qubit at different times. The amplitude was chosen such that the pulse is a π-pulse, when driving the qubit on resonance. In the pattern applied the detuning of the qubit and the pulse is varied and swept over the flux pulse. Depending on the detuning of the pulse from the qubit, it is only partially excited. One can then infer from the population of the excited stated the detuning. In order to be sensitive to the detuning, a Gaussian shaped microwave π-pulse is applied to the qubit, because it has a narrower spectrum than a square pulse. The envelope of a Gaussian pulse is given by

$$\Omega_{\mathrm{env}}(t) = Ae^{-\frac{(t-t_0)^2}{2\sigma^2}}, \tag{4.7}$$

where σ is the standard deviation and A the amplitude of the pulse centered around time $t = t_0$. On each side the pulse is truncated at $t = t_{\mathrm{c}} \pm 2\sigma$, such that the total length is 4σ.

The evolution of the qubit under such a driving pulse can be calculated in a rotating frame, which is rotating with the drive frequency ω_{d}. For example, for the Hamiltonian given in Equation (2.11) and a complex envelope, one gets

$$\hat{H}(t) = \frac{1}{2}\hbar\Delta_{\mathrm{d}}\hat{\sigma}_z + \frac{1}{2}\hbar(\Omega_{\mathrm{env}}(t)\hat{\sigma}_+ + \Omega^{\star}_{\mathrm{env}}(t)\hat{\sigma}_-). \tag{4.8}$$

Here $\Delta_d = \omega_{01} - \omega_{\mathrm{d}}$ is the detuning of the drive and the qubit. As $\Omega_{\mathrm{env}}(t)$ is real in our case and assuming $\Delta_{\mathrm{d}} = 0$, the propagator of the system reads

$$\hat{U}(t) = exp(-\frac{i}{\hbar}\int_0^t \hat{H}(\tilde{t})\,\mathrm{d}\tilde{t}) \tag{4.9}$$

$$= exp(-\frac{i}{2}\int_0^t \Omega_{env}(\tilde{t})\hat{\sigma}_x\,\mathrm{d}\tilde{t}). \tag{4.10}$$

So in order to make a π-rotation on the Bloch sphere, A has to compensate for the integral over the Gaussian. This gives $A = \sqrt{\pi}/(\sqrt{2}\sigma Erf(2))$, where $Erf(2)$ is the error function and is related to the integral over the Gaussian. The general case for $\Delta_{\mathrm{d}} \neq 0$ can simply be deduced from Equation (4.9).

For a Gaussian pulse with $\sigma = 5$ ns, which is swept over the top of a not perfectly corrected flux pulse, the result can be seen in Fig. 4.2 a. The qubit A is parked at the flux "sweet spot", where $\Phi = 0$ and linear flux noise is suppressed. It is then tuned with a flux pulse 350 MHz or 130 mΦ_0 for 50 ns. It is a square pulse with rise/fall times of 2 ns. Here Φ_0 is the flux quantum, in which the transmon is periodic. The pulse is quiet long in order to reduce the pulse bandwidth. A simulation of the measurement is shown in Fig. 4.2 b with the flux pulse given in Fig. 4.2 c. The detuning, shown in Fig. 4.2 b and c is with respect of the qubit frequency at the end of flux pulse.

As a result, one sees a clear overshoot and then 10 ns later an undershoot with a reduced amplitude of the flux pulse. The reason for the phenomena is still unclear. It could come from reflections on connectors within the cryostat.

[1] A similar work has been done in the supplement of [26]

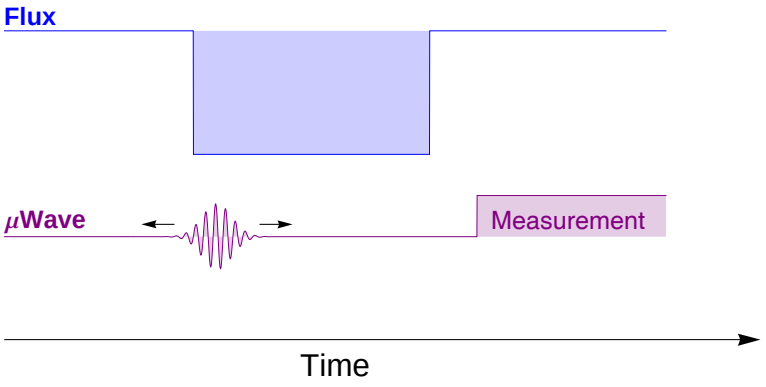

Figure 4.1: Microwave π-pulse swept over a flux pulse at different frequencies. Every point represents the $|e\rangle$-population after a Gaussian pulse centered at the corresponding time. The left picture is a measurement and the right a simulation with the qubit frequency indicated at the right hand side.

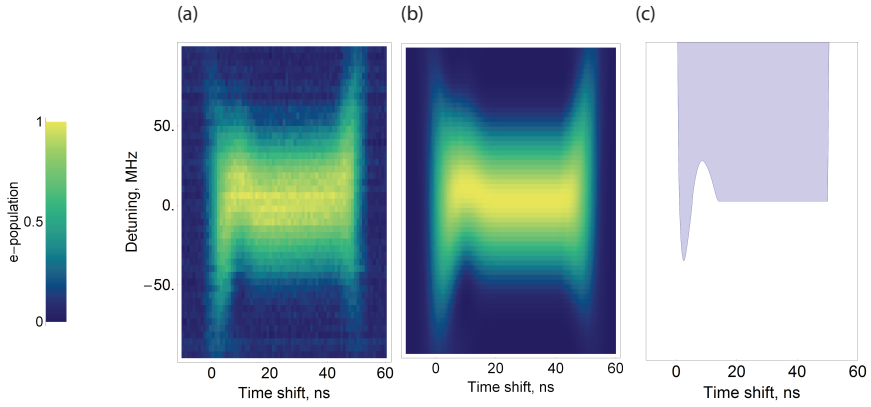

Figure 4.2: Microwave π-pulse swept over a flux pulse at different frequencies. Every point represents the $|e\rangle$-population after a Gaussian pulse centered at the corresponding time. a)Experimental result for a 20 ns long pulse. b) Simulation of the measurement, using the flux pulse given in c).

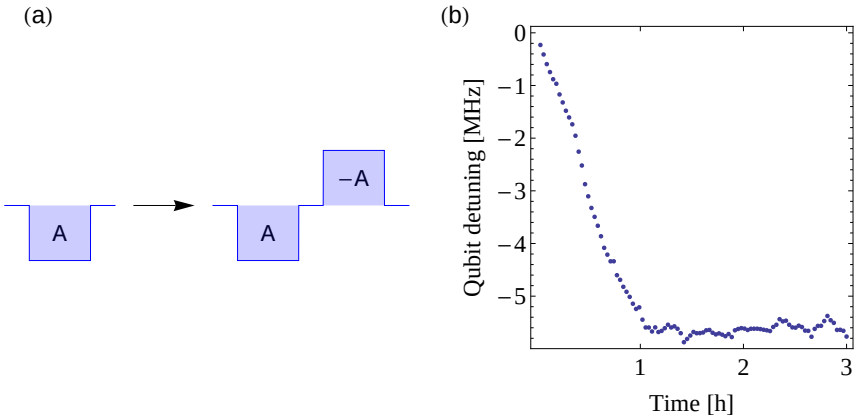

Figure 4.3: a) A flux pulse with amplitude A is replaced by two flux pulses with opposite amplitude. The average current is kept constant by adding a flux pulse with opposite amplitude. Or in other words, the integral over the current during all flux pulses is kept zero and therefore the average DC current is conserved. b) The qubit frequency 20 μs after a flux pulse of length 500ns is measured. The flux pulses are constantly applied during the whole time.

Another reason could be, that a large inductance acts as low pass filter. Such an inductance could for example be caused by a superconducting loop on the sample enclosing the SQUID loop. A changing magnetic field produced by the flux pulse induces screening currents in this loop and thus acts as low pass filter.

Therefore there are many different physical models for the overshoot. It can not be approximated by a simple under-damped oscillator, as there would be a third oscillation with reduced amplitude. The ratio of the 3$^{\text{rd}}$ amplitude to the 2$^{\text{nd}}$ would be the same as the ratio between the 1$^{\text{st}}$ and the 2$^{\text{nd}}$ amplitude. A similar argument applies for a rectangular low pass filter. In order to be correctable given by the method in Section 4.1, there should not be a zero in the spectrum. Also, the characteristic features of the response need to be in the low spectrum beneath 1 GHz. Else they would be filtered out by on board filters of the cryostat.

Another problem arises with the flux pulse on a longer timescale. The flux pulse response has a tail of roughly 200 μs. This can also be be explained by the presence of a large inductance. In order to compensate for the inductance, one can add a flux pulse with opposite amplitude. This is shown in Fig. 4.3 a. With this method the average current stays the same.

The response of many flux pulses even extends to hours. This can be seen in Fig. 4.3 b. The detuning of the qubit from its equilibrium position, 20μs after a compensated flux pulse is shown. The frequency was measured by a Ramsey experiment. The flux pulse is 500 ns long. The clear change in frequency over an hour can be attributed to heating of the sample caused by the currents used for the flux pulse generation. The heating changes the flux through the SQUID-loop. The temperature dependence of the flux is associated with spin ordering, and is further discussed in [27].

Chapter 5

Bell states and dark states

Symmetry transformation, like translation or rotation, which leaves a quantum system unchanged cause selection rules for transitions. In a system of identical atoms, the permutation invariance generates such a selection rule. Only transition between collective symmetric states are allowed [28, 29]. When these atoms are interacting with a radiation field, these symmetries cause an enhancement or suppression of spontaneous emission [28, 29, 30]. This phenomena is known as superradiance and subradiance. The subradiant state can be very robust against decoherence and is therefore very interesting for quantum information processing [30].

In circuit QED, such states have already been prepared and spectroscopically measured[28, 29]. To get the full knowledge about these states, we reconstructed their density matrix with full state tomography. Since superradiant and subradiant states are closely related to Dicke states, a short review on these states is made in Section 5.1. This is followed by a discussion of subradiance and the Purcell effect in Section 5.2. To prepare the the Dicke states in circuit QED the dispersive regime and the avoided crossing of qubits will be treated in Section 5.3 and 5.4. Depending on the symmetry of the drive, these states become dark and are covered in Section 5.6. The related Bell state production is examined in Section 5.7.

5.1 Dicke states

For a Tavis-Cummings Hamiltonian with N qubits coupled to a single mode resonator, these subradiant and superradiant qubit states are the Dicke states. In this Section we will explore the symmetries of these states and in Section 5.2 there will be an explanation, how these symmetries lead to superradiance and subradiance. The starting point is the Tavis-Cummings Hamiltonian, which reads

$$\hat{H} = \hbar\omega_r \hat{a}^\dagger \hat{a} + \hbar \sum_a \frac{\omega_a}{2} \hat{\sigma}_z^a + \hbar \sum_a g_a (\hat{a}\hat{\sigma}_{a+} + \hat{\sigma}_-^a \hat{a}^\dagger). \tag{5.1}$$

Here a is the index of the a^{th} qubit, $\hat{\sigma}_\pm = \hat{\sigma}_x \pm \imath\hat{\sigma}_y$ are the raising/lowering operators with the Pauli operators $\hat{\sigma}_{x,y,z}$ and $\hat{a}^{(\dagger)}$ are the creation/ annihilation operators of the resonator mode. The three terms describe the energy of

the resonator, the energy of the qubits and the coupling of the qubits to the resonator with coupling strength g_a, respectively.

It is instructive to rewrite the Hamiltonian (5.1) in terms of the collective angular momentum operators [31, 32]. This makes it easier to identify the states which couple to the photon field and to identify their symmetries. The radiative decay rate of these states depends crucially on the symmetries, as we will see later. The operators read

$$\hat{J}_\mu = \frac{1}{2}\sum_{a=1}^{N} \hat{\sigma}_\mu^a (\mu = x, z, y) \tag{5.2}$$

$$\hat{J}^2 = \hat{J}_x^2 + \hat{J}_y^2 + \hat{J}_z^2, \tag{5.3}$$

$\hat{J}_\mu$ are the collective angular momentum operators in the direction of μ and $\hat{J}^2$ is the total collective angular momentum operator. They have the same commutator relations as the Pauli σ_x, σ_y and σ_z operators. One can also introduce the lowering $\hat{J}_-$ and raising $\hat{J}_+$ operators by the corresponding commutator relations

$$\begin{aligned}
\hat{J}_\pm &= \hat{J}_x \pm i\hat{J}_y \\
&= \sum_{a=1}^{N} \hat{\sigma}_{\pm a} \\
\hat{J}_z &= \frac{1}{2}(\hat{J}_+\hat{J}_- - \hat{J}_-\hat{J}_+) \\
[\hat{J}_-, \hat{J}_+] &= -2\hat{J}_z \\
[\hat{J}_-, \hat{J}_z] &= \hat{J}_- \\
[\hat{J}_+, \hat{J}_z] &= -\hat{J}_+.
\end{aligned} \tag{5.4}$$

Assuming now an equal coupling strength g and transition frequency ω for all qubits, the Hamiltonian (5.1) can be written in a compact form

$$\hat{H} = \hbar\omega_r \hat{a}^\dagger\hat{a} + \hbar\omega\hat{J}_z + \hbar g(\hat{a}\hat{J}_+ + \hat{J}_-\hat{a}^\dagger). \tag{5.5}$$

This is the Hamiltonian of the Dicke model, which is a collective angular momentum model. Nevertheless, in this discussion the eigenvalues of the $\hat{J}$ operators have nothing to do with the angular momentum of the physical system. They are introduced because of the mathematical analogy of a spin $^1/_2$ system and a two level system. And it makes it much easier to study the eigenstates of the system

Because $\hat{J}_z$ and $\hat{J}^2$ commute, they can be simultaneously diagonalized and have common eigenstates. They are called Dicke states and given by $|J, M\rangle$, with $\hat{J}^2|J, M\rangle = J(J+1)|J, M\rangle$ and $\hat{J}_z|J, M\rangle = M|J, M\rangle$. These states are orthogonal, as $\hat{J}^2$ and $\hat{J}_z$ are hermitian operators. But the states can be degenerate. M can be interpreted as the energy of the states without the resonator. The energy is given by $E_M = \hbar(M + 1/2N)$. J is the cooperation number and is important for determining the collective radiation and the coupling to the resonator mode. In analogy to the angular momentum, M and J are integers or half integers. They have the constraint

$$|M| \leqslant J \leqslant \frac{N}{2}. \tag{5.6}$$

The single states are constructed by applying the raising operator J_+, which has the effect $\hat{J}_+|J,M\rangle = ((J+M)(J-M+1))^{0.5}|J,\ M+1\rangle$, $(J+M)$-times on the lowest energy state with cooperation number $J|J,-J\rangle$ and is given by

$$|J,M\rangle = \sqrt{\frac{(J-M)!}{(2J)!(J+M)!}}(\hat{J}_+)^{J+M}|J,-J\rangle. \tag{5.7}$$

To get the state $|J,-J\rangle$ we first have to discuss the degeneracy of the single states. Another reason to study the degeneracy is the following: As we will see later, the coupling to the radiation field is heavily depending on the cooperation number J. Therefor knowing the degeneracy of J is crucial.

In order to derive this degeneracy we will first investigate how many qubit states exists for an arbitrary energy, which is experimentally also important. Here we neglect J, as the energy is not depending on this quantity, and we only focus on the Hamiltonian (5.1) in this paragraph with the constraints given before, but without the resonator. For N qubits in the M^{th} excitation manifold, $N_\text{g} = \frac{N}{2} - M$ qubits are in the ground state and $N_\text{e} = \frac{N}{2} + M$ qubits are in the excited state. This also can be seen from Equation (5.3). The degeneracy of M is then simply given by the different permutations of the excitations

$$\begin{aligned} d_M &= \frac{N!}{N_\text{g}!N_\text{e}!} \\ &= \frac{N!}{(\frac{N}{2}+M)!(\frac{N}{2}-M)!}. \end{aligned} \tag{5.8}$$

To get the general degeneracy of the state $|J,M\rangle$, one can start with the degeneracy of the $|-N/2,\ -N/2\rangle$ state, which is $D_{-\frac{N}{2}} = 1$, as all qubits are in the ground state. For a state $|J,M_i\rangle$ the degeneracy does not depend on M_i, only on J[32]. Or in other words, when applying the $\hat{J}_+$ operator, which changes M, the degeneracy is conserved. So D_J denotes the degeneracy of the state $|J,M\rangle$.

At energy M, we have a degeneracy of d_M given by Equation (5.8). $D_{J=M}$ states are of the type $|\ J{=}|M|, M\ \rangle$. The others are from higher J's (Equation (5.6)) and they have the form $|\ J{=}|M|{+}1,\ M\ \rangle$, $|\ J{=}|M|{+}2,\ M\ \rangle$, ... ,$|J{=}N/2,\ M\rangle$. One gets

$$d_M = D_{|M|} + D_{|M|+1} + ... + D_{N/2}. \tag{5.9}$$

The degeneracy of the $|J,M\rangle$-state is then given by, using Equation (5.8) and (5.9)

$$\begin{aligned} D_J &= d_J - d_{J+1} \\ &= \frac{(2J+1)N!}{(\frac{N}{2}+J+1)!(\frac{N}{2}-J)!}. \end{aligned} \tag{5.10}$$

The whole degeneracy discussion is summed up in Fig. 5.1. Here the degeneracy for the cooperation number J and the energy related to M is shown. Each vertical line corresponds to an simultaneous eigenstate of the $\hat{J}_z$ and $\hat{J}^2$ operator. They are orthogonal.

Examining the dipole interaction in Equation (5.5) and the matrix element $\langle J,M|J_\pm|J',M'\rangle$, it again makes it easier to find the eigenstates of the Hamiltonian (5.5), as well to find the radiative decay rate of the state later on. One

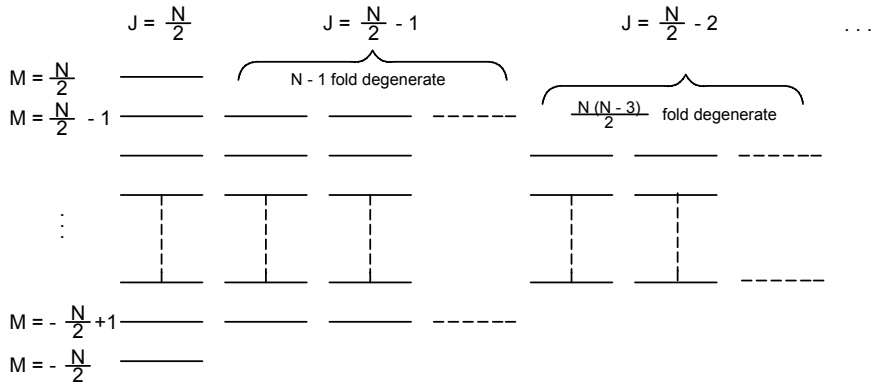

Figure 5.1: The degeneracy of the Dicke states. The degeneracy of the state $|J, M\rangle$ only depends on the cooperation number J and not on the energy associated with M.

gets the first order selection rules

$$\Delta J = 0 \tag{5.11}$$

$$\Delta M = \pm 1. \tag{5.12}$$

And one gets for the first excitation manifold of the Hamiltonian, one qubit state $|N/2, -N/2{+}1\rangle$, which couples to the photon field, as it can fulfill $\Delta M = \pm 1$. And there are N-1 qubit states $|N/2{-}1, -N/2{+}1\rangle$, which don't couple, as $\hat{J}_-|N/2{-}1, -N/2{+}1\rangle = 0$. We can introduce the notations $|n; J; M\rangle$ for a state with n photons. The first excitation manifold eigenstates can then be calculated as

$$\begin{aligned}
|\Psi_+\rangle &= \cos\theta_{\mathrm{m}}|1; N/2; -N/2\rangle + \sin\theta_{\mathrm{m}}|0; \frac{N}{2}; -\frac{N}{2}+1\rangle \\
|\Psi_-\rangle &= \sin\theta_{\mathrm{m}}|1; N/2; -N/2\rangle - \cos\theta_{\mathrm{m}}|0; \frac{N}{2}; -\frac{N}{2}+1\rangle \\
|\Psi_0\rangle &= |0; \frac{N}{2}-1; \frac{N}{2}-1\rangle,
\end{aligned} \tag{5.13}$$

with the mixing angle θ_{m} defined by $\cos 2\theta_{\mathrm{m}} = -\Delta/\sqrt{4(\sqrt{N}g)^2 + \Delta^2}$ and $\Delta = \omega_a - \omega_{\mathrm{r}}$. One can see that the coupling of the collective state $|N/2, -N/2{+}1\rangle$ to the resonator is enhanced by the square root of the number of qubits to $\sqrt{N}g$. The state $|\Psi_0\rangle$ is N-1 times degenerate. So we have 2 states which are dressed with the resonator and N-1 states which are pure qubit states and have no radiative decay channel into the resonator, see Section 5.22. The energies

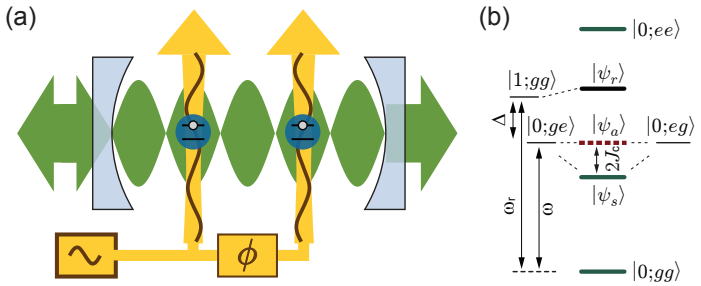

Figure 5.2: 2 Qubits in resonance in the dispersive regime. a) schematic drawing of the experiment with 2 drives on the qubit b) Energy levels for the 2 qubits and the characteristic energy splitting $2J_c$ in the dispersive regime, which is discussed in Section 5.3.

can be found analytically:

$$\begin{aligned} E_+ &= \hbar(\omega_\mathrm{r} + \frac{\Delta + \sqrt{\Delta^2 + 4(\sqrt{N}g)^2}}{2}) \\ E_- &= \hbar(\omega_a - \frac{\Delta + \sqrt{\Delta^2 + 4(\sqrt{N}g)^2}}{2}) \\ E_0 &= \hbar\omega_a. \end{aligned} \tag{5.14}$$

In order to clarify the concepts introduced we will have a look on the case with two and three qubits. This treatment is also important as most of the experiments are conducted with this number of qubits. For N=2 qubits in resonance the first excited manifold states (5.13) can be rewritten in a notation using the population of the qubits. It is shown here because this population will get measured later on in the experiment, when characterizing the states. The states read

$$\begin{aligned} |\Psi_+\rangle &= \cos\theta_\mathrm{m}|1;gg\rangle + \sin\theta_m|0;\Psi_s\rangle \\ |\Psi_-\rangle &= \sin\theta_\mathrm{m}|1;gg\rangle - \cos\theta_m|0;\Psi_s\rangle, \\ |\Psi_0\rangle &= |0;\Psi_\mathrm{m}\rangle, \end{aligned} \tag{5.15}$$

where $|\Psi_{s,a}\rangle = 1/\sqrt{2}(|ge\rangle \pm |eg\rangle)$ are the symmetric and the antisymmetric state. The symmetric state $|\Psi_s\rangle = |J = 1, M = 0\rangle$ can be changed into the ground $|gg\rangle = |1, -1\rangle$ and the double excited state $|ee\rangle = |1, 1\rangle$ with the $\hat{J}_\pm$ operators. This states are therefore called triplet states. The antisymmetric state $|0, 0\rangle$ is a singlet state, as it does not couple to any other state. The corresponding energies in the dispersive limit are shown in Fig. 5.2, for a large detuning $g/\Delta \ll 1$.

The N=2 case is quite simple, as one works with the symmetric and the antisymmetric state and no states are degenerate. For the the N=3 case it becomes a little bit more tricky, because the $|J = \frac{1}{2}, M = \frac{1}{2}\rangle$ state is now degenerated. The symmetric state $|\frac{3}{2}, \frac{1}{2}\rangle$ is simply obtained by acting with the creation operator $\hat{J}_+$ on the ground state. The $|\frac{1}{2}, \frac{1}{2}\rangle$ can be represented by any state of the form

$$|\Psi_a\rangle = c_1|egg\rangle + c_2|geg\rangle + c_3|gge\rangle, \tag{5.16}$$

with $c_1+c_2+c_3 = 0$ and the normalization $|c_1|^2+|c_2|^2+|c_3|^2 = 1$ [32]. Obviously this state is degenerated. The symmetric state $|\frac{3}{2}, \frac{1}{2}\rangle$ is called W-state and reads

$$|\Psi_s\rangle = \frac{1}{\sqrt{3}}(|egg\rangle + |geg\rangle + |gge\rangle). \tag{5.17}$$

A longer discussion of this state can be found in Chapter 6.

The so far discussed states can all be made nicely symmetric or antisymmetric. This changes when the couplings are not equal anymore. In the following paragraph we will have a short look on this case. It is important, as on our sample the coupling doesn't seem to be equal. The interaction between the resonator and the qubits is given in Hamiltonian (5.1). One can again define operators in analogy to Equation (5.4)

$$\hat{J}^{\diamond}_{\pm} = \sum_a g_a \hat{\sigma}_{\pm a}. \tag{5.18}$$

And the interaction then reads similar as in Equation (5.5):

$$\hat{H}^{\diamond}_{int} = \hbar(\hat{a}\hat{J}^{\diamond}_{+} + \hat{J}^{\diamond}_{-}\hat{a}^{\dagger}). \tag{5.19}$$

Again one can get the coupling between the resonator and single states by examining the effect of the $\hat{J}^{\diamond}_{-}$ operator. An arbitrary qubit state of the first excitation manifold can be written as

$$|\Psi^{\diamond}\rangle = c_1|eg...g\rangle + c_2|geg...g\rangle + ... + c_N|g...ge\rangle, \tag{5.20}$$

with the normalization $\sum_a |c_a|^2 = 1$. Here the photonic part is not included. In order to investigate the eigenstates of the Hamiltonian (5.19), one can have a look on the impact of $\hat{J}^{\diamond}_{-}$. The kernel $span\{|\Psi^{\diamond}\rangle \,|\, \hat{J}^{\diamond}_{-}|\Psi^{\diamond}\rangle = 0\}$ is given by the condition

$$c_1 g_1 + ... + c_N g_N = 0. \tag{5.21}$$

It is simply found by acting $\hat{J}^{\diamond}_{-}$ on $|\Psi^{\diamond}\rangle$. There exists N-1 linear independent states, which fulfill this condition. If this states are extended by a photonic part, which is zero, they are eigenstates of the interaction Hamiltonian (5.19), with eigenvalue 0, and of the Hamiltonian (5.1). They don't couple to the radiation field.

To find the state, which couples to the resonator, one can apply $\hat{J}^{\diamond}_{+}$ to the ground state $|g...g\rangle$. Like this one can examine the effect of the Hamiltonian 5.19. One gets the condition,

$$\frac{c_1}{g_1} = ... = \frac{c_N}{g_N} = c, \tag{5.22}$$

for the state which couples to the resonator. The constant c is related to the normalization and given by $c = 1/(\sum_a |g_a|^2)^{0.5}$. One can see from Equation (5.22) and (5.21), that this state is orthogonal to the states described before.

The main point of this discussion, is that nothing really changes when the coupling strengths g_a are not equal anymore. The only slight differences are, that the states don't have anymore nice symmetrical properties. And the energy

and the mixing angle between the qubit state and the photonic state are altered. They are given by

$$E_+ = \hbar(\omega_\mathrm{r} + \frac{\Delta + \sqrt{\Delta^2 + 4(1/c)^2}}{2})$$
$$E_- = \hbar(\omega_a - \frac{\Delta + \sqrt{\Delta^2 + 4(1/c)^2}}{2})$$
$$E_0 = \hbar\omega_a. \tag{5.23}$$

And the mixing angle between the qubit state and the photonic state $|1; g...g\rangle$ is given by $\cos 2\theta_m = -\Delta/\sqrt{4(1/c)^2 + \Delta^2}$

5.2 Superradiance and Purcell effect

The phenomena of superradiance was first studied by Dicke in 1954 for N two level atoms. He predicted, that for an ensemble of N atoms their radiation could be enhanced or suppressed. This is due to the collective coupling over the resonator.

For a given initial Dicke state $|i\rangle$ of N 2-level atoms and all field modes are in the vacuum state, the rate R for the transition to the final state $|f\rangle$ by emitting one photon of frequency ω_r is given by Fermi's golden rule [31]. For a normal dipole interaction of atoms, one finds that the transition rate R is proportional to the matrix element squared $R \propto |\langle f|\hat{J}_-|i\rangle|^2$. For Dicke state, this is given by $\langle f|\hat{J}_-|i\rangle = ((J+M)(J-M+1))^{0.5}$. This results in

$$R = A(J+M)(J-M+1), \tag{5.24}$$

where A is the Einstein A coefficient and is the spontaneous emission rate of a single atom into the vacuum. For the ground state J=N/2 and M=-N/2 one gets the emission rate 0 as expected. For all atoms excited, J=N/2 and M=N/2, one gets R=N A, as one would expect for N independent atoms.

When not all atoms are excited, the radiance is either enhanced (superradiance) or suppressed (subradiance). For example for M=0, half of the atoms are excited. If J(J+1)$\approx N^2/4$ one gets superradiance and the decay rate is enhanced by a factor of N. For $J \approx 0$ the radiation is highly suppressed resulting in subradiance.

The effect of superradiance and subradiance also influences the decay rate of the transmon coupled to a resonator, described by the Hamiltonian (2.16). In our experiment it is given by $\gamma = \gamma_\kappa + \gamma_\mathrm{i}$, γ_i is associated with non-radiative, intrinsic decay and γ_κ with the radiative decay. The radiative decay is mainly coming from the Purcell effect and not from dipole interaction to free space [33, 18, 28]. During the Purcell relaxation the photonic part of the qubits, decays through the resonator into free space. It is coming from the coupling of the resonator to an external photon bath, which includes the external transmission line. The interaction can be described by the Hamiltonian

$$H_\kappa = \hbar \sum_k \lambda_k [\hat{b}^\dagger \hat{a} + \hat{a}^\dagger \hat{b}], \tag{5.25}$$

where $\hat{b}^\dagger$ and $\hat{b}$ are creation and annihilation operators of the photon reservoir and the coupling of the resonator to the k^{th} mode is given by the coupling

strength λ_k. To calculate the transition rate, one can use Fermi's golden rule and a continuum limit [18]. The result for the one photon loss is

$$\gamma_\kappa^{i,f} = \frac{2\pi}{\hbar} p(\omega_k) |\sum_{k'} \lambda_{k'} \langle 1_k, f | [\hat{b}^\dagger \hat{a} + \hat{a}^\dagger \hat{b}] | 0, i \rangle|^2. \tag{5.26}$$

Here the photon of the resonator has a frequency of ω_r. $p(\omega_k)$ is the bath's density of states at energy $\hbar\omega_k$. κ can be defined as $\kappa = 2\pi\hbar p(\omega_k)|\lambda|^2$, which gives

$$\gamma_\kappa^{i,f} = \kappa |\langle f | \hat{a} | i \rangle|^2. \tag{5.27}$$

In order to suppress this decay one can operate in the dispersive regime. To investigate this, qubit A and B of our sample were tuned in resonance at the sweet spot of qubit B. For the relaxation times, one gets with Equation (5.15),

$$\gamma_\kappa^{\Psi_0} \approx 0 \tag{5.28}$$

$$\gamma_\kappa^{\Psi^-} \approx \kappa \sin^2 \theta_\mathrm{m} \approx 20kHz, \tag{5.29}$$

from the dressing. The measured values of the energy relaxation time $T_1 = 1/\gamma$ is $T_1^0 = 890 \pm 60$ ns and $T_1^- = 764 \pm 74$ ns. The times are found, by measuring the decay over $1\mu s$, which is quiet short. The decay does not seem to be governed by the Purcell effect. However, this drastically changes, when the qubits are not anymore far detuned from the resonator and the Purcell effect plays a role [34]. Also in this analysis the Hamiltonian (5.1), instead of (2.16) is used.

5.3 Dispersive regime

As the transmons are operated in the dispersive regime, this section discusses the dispersive regime of the Hamiltonian (5.1). In contrast to the Hamiltonian (2.16), there is a restriction to two levels, as we are only interested in them. Similar to Section 2.2.5, the direct qubit-resonator interaction can be perturbatively eliminated by using a Schrieffer-Wolf transformation and the Housdorf expansion [35, 7].

$$\begin{aligned} \hat{H} &= \hbar\omega_\mathrm{r} \hat{a}^\dagger \hat{a} \\ &+ \frac{\hbar}{2} \sum_a (\omega_a + \chi_a + 2\chi_a \hat{a}^\dagger \hat{a}) \hat{\sigma}_{z,a} \\ &+ \hbar \sum_{a',a} J_{a',a} (\hat{\sigma}_{a',-} \hat{\sigma}_{a,+} + \hat{\sigma}_{a,-} \hat{\sigma}_{a',+}) \end{aligned} \tag{5.30}$$

Here the first term is the normal resonator frequency. In the second term we get the qubit energies with a "Lamb" shift $\chi_a = g_a^2/\Delta_a$ with $\Delta_a = \omega_a - \omega_\mathrm{r}$ and an "AC-Stark" shift $(2\chi_a n)$ due to the presence of photons[7]. The Stark shift can also be seen as a qubit dependent shift of the cavity frequency.

In the third term of (5.1), we get an effective flip-flop coupling of the single qubits via virtual photons. This is called $J_{a',a}$-coupling or dispersive exchange coupling. This should not be mixed up with the total angular momentum number J in the previous chapter. The dispersive coupling is therefore denoted by

two subscripts $J_{a',a}$. $J_{a',a}$ and given by

$$J_{a',a} = \frac{1}{2} g_{a'} g_a \left(\frac{1}{\Delta_{a'}} + \frac{1}{\Delta_a}\right). \tag{5.31}$$

This mechanism can be used to entangle qubits and gives an anticrossing of the excited qubit levels. The anticrossing is discussed in depth in Section 5.4.

5.4 Dispersive qubit-qubit interaction

In order to investigate the Dicke states of two qubits one has to tune the qubits in resonance. This leads to an avoided crossing of the energy levels. One can use the Hamiltonian in Equation (5.30) to analysis the anticrossing. The avoided crossing is governed by the dispersive coupling strength $J_{1,2}$.

In order to find the dispersive coupling strength $J_{1,2}$ and the resonance of two arbitrary qubits, named 1 and 2, the following procedure is applied: One qubit, say qubit 1, is tuned by changing the flux Φ with external coils. The energy of the qubit is approximately changing linearly. As a single coil couples to all qubits two coils are used, in order to keep the flux at the second qubit constant. The qubit frequencies and the dispersive coupling strength are extracted from a fit to the energies:

$$E_{\pm}(\omega_1^{\mathrm{ge}}, \omega_2^{\mathrm{ge}}, J_{1,2}) = \hbar\left(\frac{\omega_1^{\mathrm{ge}} + \omega_2^{\mathrm{ge}}}{2} \pm \frac{\sqrt{(\omega_1^{\mathrm{ge}} - \omega_2^{\mathrm{ge}})^2 + 4J_{1,2}^2}}{2}\right) \tag{5.32}$$

Here $\omega_i^{\mathrm{ge}} = \omega_i + \chi_i$ is the Lamb shifted energy of the i^{th} qubit. ω_1^{ge} is a linear function of the magnetic flux. The energy of the second qubit is ω_2^{ge} and constant.

This procedure was done for qubit A and B, by keeping qubit B constant, see Fig. 5.3. For each flux bias the qubit frequencies were measured with pulsed spectroscopy. One sees the avoided crossing due to the transverse exchange coupling, with a minimum frequency difference of $2J_{\mathrm{A,B}}$. At the upper level, there is a reduction of the transmission amplitude during the crossing. In the middle, is the 2 photon process to the $|ee\rangle$-level.

Fitting this data to the previously discussed formula, one finds $J_{\mathrm{A,B}} = 25.1 \pm 1.4$ MHz and $\omega_B^{\mathrm{ge}} = 6.06(53)$ GHz. Calculating the $J_{\mathrm{A,B}}$-coupling from formula (5.31) with the numbers given in Section 3.1, results in $J_{\mathrm{A,B}} = 42.1$ MHz. higher order resonator modes [34] can partially account for this deviation. Another reason for the deviation is the qubit frequency dependence of the coupling $g_a \propto \langle g|\hat{n}|e\rangle \propto \sqrt{\omega_a}$ [36], which was neglected when measuring the coupling strengths of the qubits.

The effectiveness of this method was checked by the use of flux pulse and Ramsey experiments. When the qubits are in resonance according to the fit, one qubit was tuned out of resonance and the dispersively shifted frequency of the fixed qubit is measured with a Ramsey Measurement. The pattern can be found in Fig. 5.4.

In a Ramsey experiment the qubit is first prepared in the ground state. A slightly detuned $\pi/2$ pulse around the x-axis ($R_x^{\pi/2}$) is then applied, which rotates the qubit state into the equatorial plane of the Bloch sphere. In a frame, rotating with the drive frequency, the qubit state then rotates around

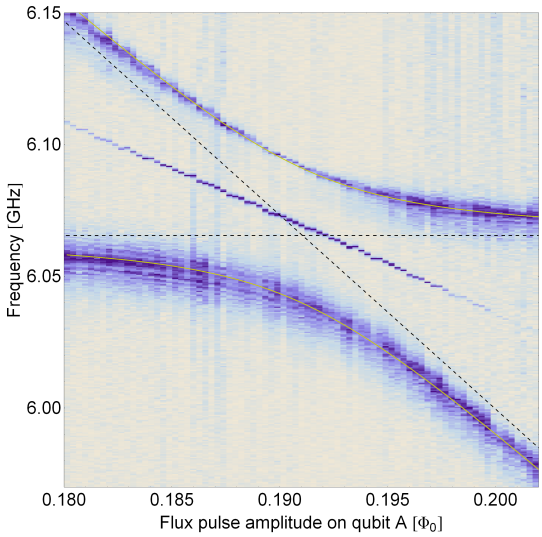

Figure 5.3: Avoided crossing between qubit A and B. The energy levels as a function of flux on qubit A are plotted. The yellow is a fit to the energy levels, the black dashed lines are the transition frequencies of the dispersively shifted qubits without J-coupling.

the z-axis with a frequency determined by the detuning. After a time Δt, a second $\pi/2$-pulse around the x-axis is applied. The phase picked up during the time Δt is called dynamical phase. Depending on the amount of dynamical phase accumulated, the pulse around the x-axis rotates the qubit to the ground or to the excited state. From the measured qubit population as a function of time Δt, the detuning and the qubit frequency can be inferred.

For the given anticrossing the qubits are found to be in resonance with an accuracy of about 1 MHz. The dispersively shifted qubits then form the symmetric and the antisymmetric state due to the $J_{\mathrm{A,B}}$ coupling. These states are maximally entangled.

If the states are not totally in resonance and detuned by $\delta = \omega_{\mathrm{A}}^{\mathrm{ge}} - \omega_{\mathrm{B}}^{\mathrm{ge}}$, the eigenstate of the Hamiltonian (5.30) are then given by

$$\begin{aligned} |\Psi_{\mathrm{u}}\rangle &= \sin\theta_{\mathrm{m}}|eg\rangle + \cos\theta_{\mathrm{m}}|ge\rangle \\ |\Psi_{\mathrm{l}}\rangle &= \cos\theta_{\mathrm{m}}|eg\rangle - \sin\theta_{\mathrm{m}}|ge\rangle. \end{aligned} \tag{5.33}$$

θ_m is the mixing angle and given by $\cos 2\theta_{\mathrm{m}} = -\delta/\sqrt{4J^2+\delta^2}$ and $\sin 2\theta_{\mathrm{m}} = 2J/\sqrt{4J^2+\delta^2}$. $|\Psi_{\mathrm{u}}\rangle$ is the state of the upper energy level and $|\Psi_{\mathrm{l}}\rangle$ of the lower, if $J_{\mathrm{A,B}}$ is positive. For large detuning $|\delta| \gg J_{\mathrm{A,B}}$, the single qubit states are recovered.

Having a closer look on the anticrossing, not from the perspective of the dispersive Hamiltonian, but from the normal Tavis-Cummings Hamiltonian (5.1), the picture doesn't changes much. In Fig. 5.5, the absolute amplitude of the single basis vectors for qubit A $|0;eg\rangle$, qubit B $|0;ge\rangle$ and the resonator $|1;gg\rangle$ are shown. The asymmetry of the resonator-qubit coupling is taken from Section 3.1 and assumed to have opposite sign, which is discussed in the next section. On the x-axis, the detuning of the Lamb shifted frequencies is shown.

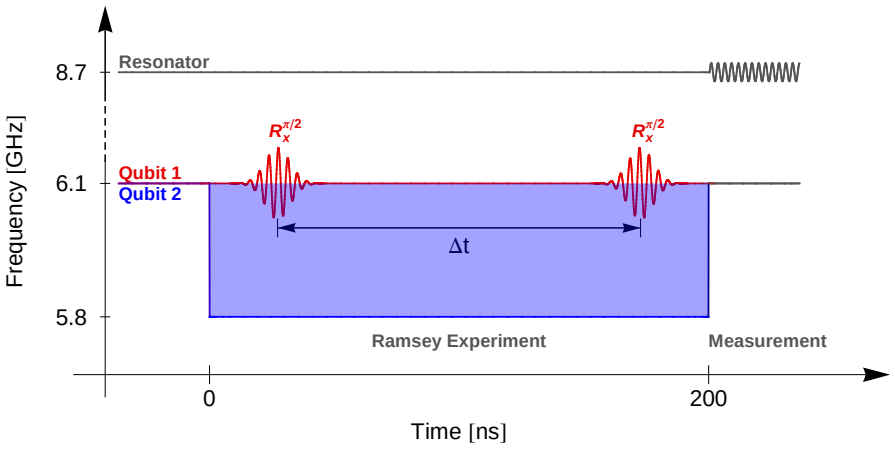

Figure 5.4: Ramsey type measurement: qubit 1 is kept constant at the same frequency. Qubit 2 is tuned out of the resonance by a flux pulse (blue). During this, a Ramsey measurement is performed on qubit 1 to determine its frequency.

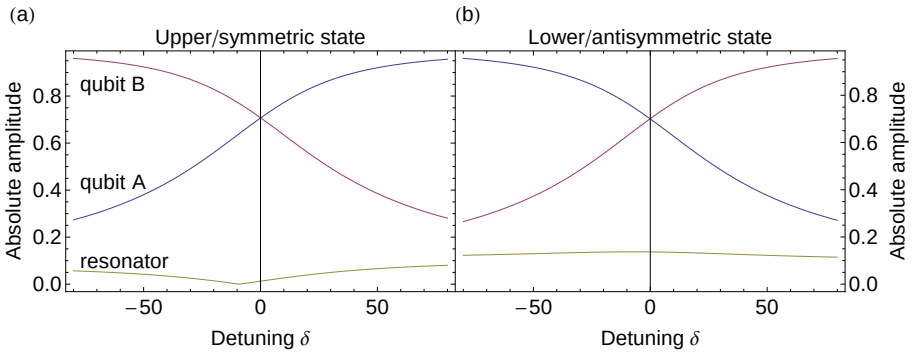

Figure 5.5: The states at the anticrossing: a) Symmetric upper state has a very small photonic component. b) Antisymmetric state, couples to the resonator, due to different sign of the coupling.

Although we have Dicke states, they both have a dressing. This is due to the coupling asymmetry discussed in Section 5.1 and the bare qubit frequencies are not in resonance. At $\delta = 0$ the bare qubit frequencies have a difference of $\omega_\mathrm{A} - \omega_\mathrm{B} = \chi_\mathrm{A} - \chi_\mathrm{B}$. Also at this point the energy difference between the states is at a minimum. So one has to note from this pictures, that for the anticrossing, the difference between the Lamb shifted frequencies is important and not the bare qubit frequencies.

5.5 Dark states

Another feature of Dicke states, beside superradiance, is the forming of dark states for drives. Their decay can be made small, as seen in the the last Section, but also they can be hard to populate. Dark stakes are defined by

$$\langle gg|H_\mathrm{d}|\Psi_\mathrm{dark}\rangle = 0, \tag{5.34}$$

for an external drive H_d. The vanishing of the matrix element is highly dependent on the symmetry of the drive and of the state. First we investigate a drive which is applied through the resonator. This drive can be written in an rotating frame, rotating with the drive frequency ω_d [34, 35, 10]:

$$H_d = \frac{\epsilon}{|\omega_\mathrm{r} - \omega_d|}(\sum_a g_a \sigma_+^a + H.c.), \tag{5.35}$$

ϵ denotes the drive strength. The relative sign of the coupling strengths g_a are conditioned on the symmetry of the electromagnetic wave inside the resonator. Depending on this symmetry, the relative sign of the electromagnetic field will change at the single places of the qubits. In the case of our resonator with the fundamental mode $\omega_0 = c_\mathrm{eff}/2L$, this can be seen in Fig. 5.6. Here, L is the length of the cavity and $c_\mathrm{eff} \approx c/\sqrt{5.5}$ is the effective speed of light in the transmission line. The phase difference is then given by $\Delta\phi = \omega_\mathrm{d} L/c_\mathrm{eff}$.

For the two qubits A and B in resonance, driven beneath the first fundamental mode, the g_a have opposite signs. Since H_d can only drive transitions from the ground state $|gg\rangle$ to states that reflect the same symmetry as H_d, the antisymmetric state $|\Psi_\mathrm{a}\rangle$ is bright and the symmetric state $|\Psi_\mathrm{s}\rangle$.

A drive with an arbitrary symmetry will present a different picture. It reads for two qubits

$$H_\mathrm{d} = \epsilon\hbar(\hat{\sigma}_+^1 + \xi e^{i\phi}\hat{\sigma}_+^2) + H.c., \tag{5.36}$$

where ξ is again the drive strength and ξ is the difference of the two drive strength on the two qubits. The phase difference of the two drives, which influences the symmetry of the drive, is denoted by ϕ. The schematic of the experiment can also be seen in Fig. 5.2 a. The matrix element for the symmetric and the antisymmetric state can then be written as [28]

$$|\langle gg|H_\mathrm{d}|\Psi_\mathrm{s/a}\rangle| = \epsilon\hbar\sqrt{\frac{1 + \xi^2 \pm 2\xi\cos\phi}{2}}. \tag{5.37}$$

If the drive is neither symmetric nor antisymmetric, it couples $|gg\rangle$ to both states. For two qubits in resonance this can be seen in Fig. 5.7. The measurement was made with pulsed spectroscopy: After a 500 ns long saturation pulse, the measurement tone is switched on and the transmitted signal is measured.

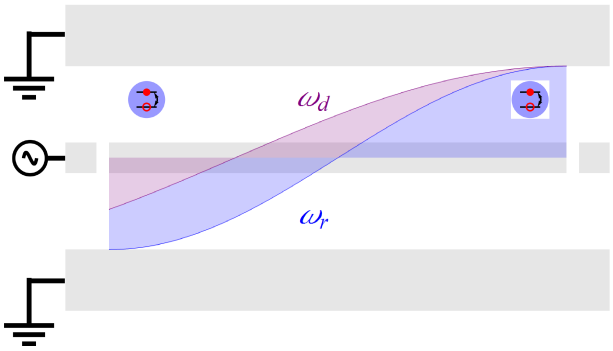

Figure 5.6: The fundamental resonator mode ω_r has opposite sign of electromagnetic field at the end of the resonator. For our experiments the qubits were placed here. When a drive with frequency ω_d, approximately the same as ω_r, is applied through the resonator, it has approximately the same symmetry as the fundamental mode.

Here the drive is applied on the single qubits. The upper state has a dark state at 0.6 2π and the lower state at 0.14 2π. A reason for the not perfect phase difference of 0.5 2π might be the different cable lengths of the drive line. Further discussion of the topic can be found in [28]. This dark states are not due to limited bandwidth of the resonances and therefore a resolution problem of the spectroscopy, which has been verified in different experiments.

5.6 Tomography of Dark and Dicke states

We now have all the tools to examine the dark states. The states which are dark to a drive applied to the resonator can be found again by measuring the anticrossing between the qubits with the corresponding drive, see Fig. 5.8. The upper state is the symmetric state, as the coupling to the resonator has opposite signs, and the lower state is the antisymmetric state. The wobbling of the lines coincide with thermal fluctuations of the cryostat, which's origin are unknown. The shifting of the dark state can be explained by the different coupling amplitude, as seen in Fig. 5.6. The qubits can than be tuned into resonance using the formula of Equation (5.32).

We can then drive Rabi oscillations between the ground state and first excitation manifold. This is done over the gatelines in order to select the phase difference of the drive between the single qubits. In Fig. 5.9 a one can see the Rabi oscillations for Gaussian microwave pulse of different length, but with the same amplitude (Equation (4.7)). The Gaussian pulse is truncated after 2 σ, such that it has a length of 4 σ, as discussed in Section 4.2. One can see that the oscillations for the two one-excitation states at 6.04 GHz and 6.09 GHz are excited during the Rabi oscillation. Whereas the double excitation state $|ee\rangle$ is only partially excited as we can see later. The phase difference of the drive at the two gate lines is in favour of the upper state, and the Rabi oscillation has a higher frequency.

In Fig. 5.9 b Rabi oscillation between the ground state $|gg\rangle$ and the anti-

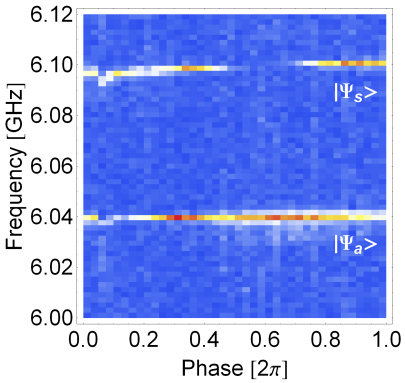

Figure 5.7: Phase dependence of the Transmission amplitude, as a function of the drive frequency ω_d. When the two qubit are in resonance, the phase dependence on the drive of the two 2-qubit states gives two dark states. They are phase shifted by roughly π.

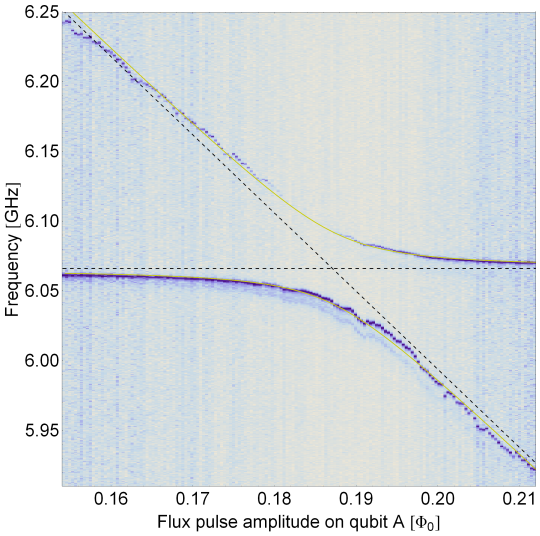

Figure 5.8: Avoided crossing between qubit A and B driven through the cavity. This gives a dark state around the anticrossing.

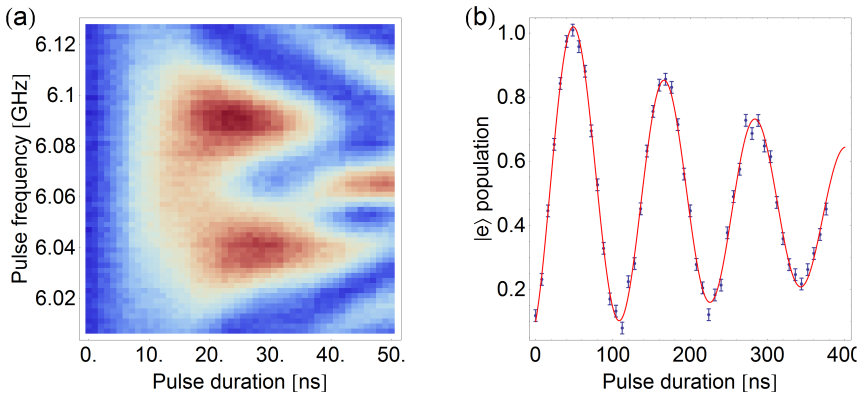

Figure 5.9: Rabi oscillations of the qubits in resonance, a) Rabi oscillations for Gaussian pulse with different length. The upper state is at 6.09 GHz and the lower is at 6.04 GHz. b) Rabi oscillation of the upper state with Gaussian pulse of different length.

symmetric state at frequency 6.09 GHz using square pulses with varying length is shown. This is the symmetric state. Due to broader bandwidth of the square pulse, the amplitude is reduced. Therefore the Rabi frequency is smaller. Due to decoherence effects the amplitude of the Rabi oscillation decays with an exponential envelope. For the square pulse, as well as for the Gaussian pulse, the rotation on the Bloch sphere is linear in the pulse length. This can be seen from Equation (4.9). From both pictures, one can see, that the single states can be driven individually. Using a pulse length, that corresponds to half a period of the Rabi oscillations, we can then prepare the symmetric or the antisymmetric state.

To get the density matrix ρ, state tomography was applied, which is shortly revised here: With a single measurement of the qubit state is not possible to extract its full information, as the state gets projected on the eigenstates of the measurement operator. It is thus only possible to determine one component of the Bloch sphere exactly, but the other two components remain totally unknown. This problem can be solved by the quantum state tomography. Here the state is prepared many times. The projection of the state on the different Bloch sphere axes are determined. But instead of changing the measurement and measuring the projection on each axis, one rotates the states. Now, the projection on the same axis is measured. Hence, one can infer the projection on all the other axis. In this way, the density matrix ρ can be determined to arbitrary precision.

There is a major draw back of this procedure: The physical state is inferred by linear inversion and this is prone to measurement errors. The calculated density matrices are normally not physical, usually meaning not positive-semidefinite and not normalized. One can get the physical state with a maximum likelihood procedure [37, 38]. Normally, these procedures are non trivial and involve iterative methods. These methods are an active topic of research [39].

To make a tomography of the states in resonance, the qubits have to be tuned

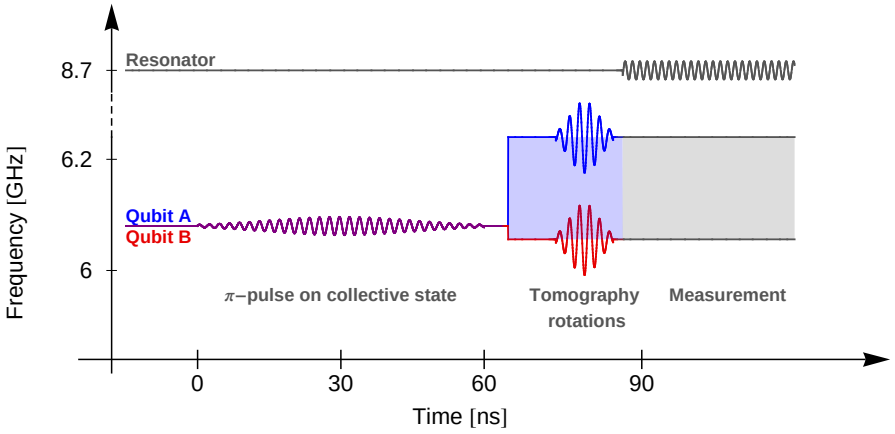

Figure 5.10: Excitation of a collective state, when the qubits are in resonance and characterization with quantum state tomography.

out of resonance, in order to address the qubits separately. The detuning should be fast, due to decoherence effects of the states. The detuning is done with a flux pulse. The corresponding pattern can be found in Fig. 5.10. The collective state is driven with a 60 ns long Gaussian pulse with a standard deviation of $\sigma = 15$ ns. The length of the pulse is chosen such that the $|ee\rangle$-level does not get populated. The qubits are then tuned 180 MHz out of resonance. The qubits are rotated by 12ns long tomography pulses. These pulses are DRAG-pulses in order not to populate other states and they are discussed in [40]. Between the microwave pulses on the qubits and the start of the fluxpulse we add a 15ns long time buffer. This ensures that the microwave pulse does not overlap with the overshoot and undershoot of the flux pulse discussed in Section 4.2.

The reconstructed density matrices after applying the max. likelihood method are shown in Fig. 5.11 for the symmetric state in Fig. 5.11 a and for the antisymmetric state in Fig. 5.11 c. Qubit A was rotated by 0.14π on the x,y-Plane of the Bloch sphere. This was done in both cases after the data processing, in order to compensate for dynamical phase errors. Also there was a compensation of the finite detuning during the state tomography, which is discussed in the second half of this section.

In Fig. 5.11 b and d are the Pauli sets which show the expectation value for the observables deduced from Pauli operators, discussed in [41]. And the theoretical stabilizers for the symmetric and the antisymmetric states are indicated. The stabilizers are elements of the Pauli group, which leave the state unchanged. The symmetric state and the antisymmetric state are produced with a fidelity of 85% and 93%.

In the plots, the first thing to notice is the population of the ground state. This can be accounted by a slightly off resonant drive of 2.5 MHz. For a detuned 60ns Gaussian pulse, the ground state population rises to 0.05. The limiting factor for shortening this pulse is the population of the $|ee\rangle$-level by 2 photon transitions. Also the not perfectly calibrated amplitude of a π-pulse can account for this ground state.

The ground state population is influenced by the decay of the qubits, too.

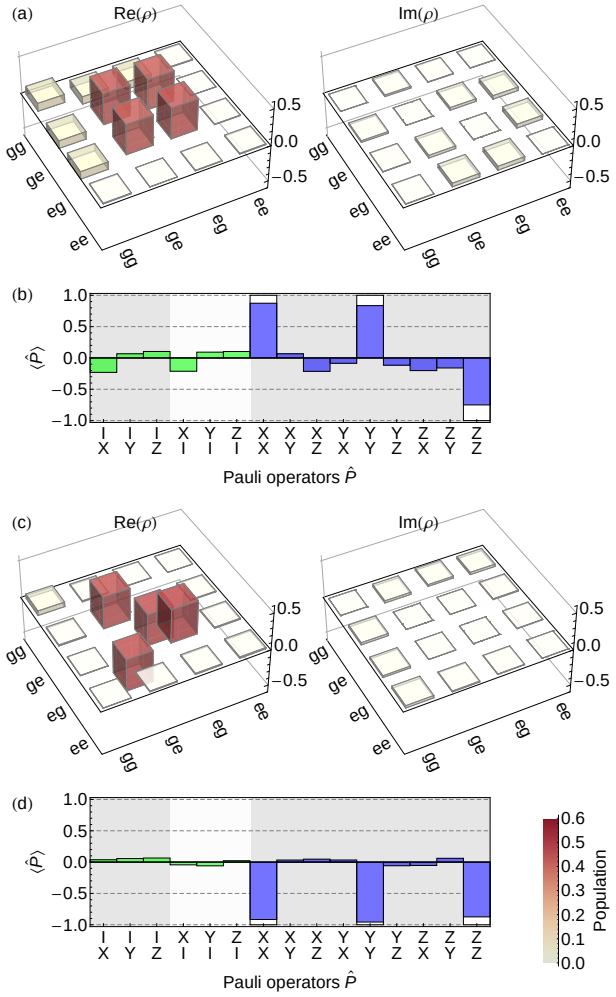

Figure 5.11: Collective states, when the two qubits A and B are in resonance. a) Real and imaginary part of the upper state density matrix. b) Pauli set of the upper state, compared with the symmetric state. c) Real and imaginary part of the lower state density matrix. d) Corresponding Pauli set is compared with an antisymmetric state.

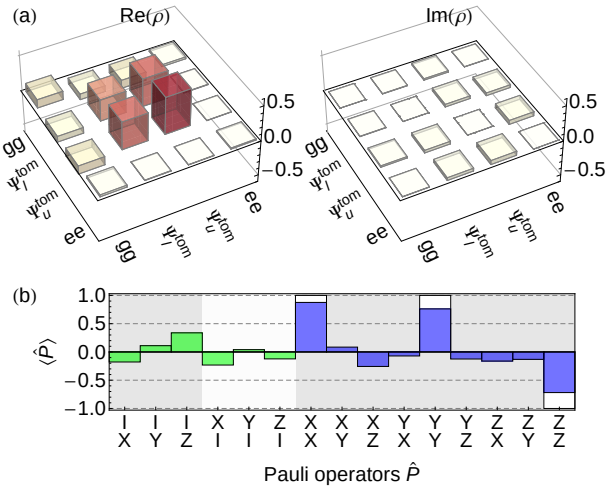

Figure 5.12: Original data of the symmetric state with no compensation of the finite detuning.

This mechanism contributes with the same order of magnitude as the detuning. The corresponding numbers can be found in Section 5.2. The result of the decay is a mixed state. This in contrast to the off resonant drive, where the result is a pure state. The process can therefore be distinguished with the help of the off-diagonal elements. The symmetric state is driven slightly off-resonant, whereas the ground population of the antisymmetric is governed by the decay.

Another error source for the $|gg\rangle$ state is the state tomography: A prepared ground state is reconstructed with a fidelity of 97.5%. This error could account for the fallowing factors: One is the not perfect flatness of the flux pulse during the tomography. Therefore the single gates are not perfect. The other is, that qubit A is not operated at the flux sweetspot and is therefor prone to fluxnoise, which affects the quality of the single tomography rotations.

Now we want to investigate the effect of the finite detuning on the state tomography. The detuning during the state tomography was 180 MHz. The low detuning is chosen, in order not to heat the sample too much. This heating is discussed in Section 4.2. The rather low detuning implies a remaining entanglement between the single states. It has a impact on the state tomography, which one can not be neglect. In the next few paragraphs this remaining mixture and its effect on the state tomography will be examined.

In an ideal situation, the eigenbasis of the system during the state tomography are the product states $|gg\rangle$,$|eg\rangle$,$|ge\rangle$ and $|ee\rangle$. Applied tomography pulses then only affect a single qubit. If there is a finite detuning, the eigenbasis is $|gg\rangle$, $|\Psi_{\mathrm{u}}^{\mathrm{tom}}\rangle = \alpha|eg\rangle + \beta|ge\rangle$,$|\Psi_{\mathrm{l}}^{\mathrm{tom}}\rangle = \beta|eg\rangle - \alpha|ge\rangle$ and $|ee\rangle$ due to the dispersive qubit-qubit coupling. The coefficients α and β are found from Equation (5.33). The tomography rotation then acts on the corresponding eigenstates of the system.

On first sight this mixing doesn't seem to affect the state tomography a lot: According to Equation (5.33), the lower state $|\Psi_{\mathrm{l}}^{\mathrm{tom}}\rangle$ has a mixing of $\alpha^2 = 97.5\%$ with qubit B and $\beta^2 = 2.5\%$ with qubit A. This can be seen from Equation

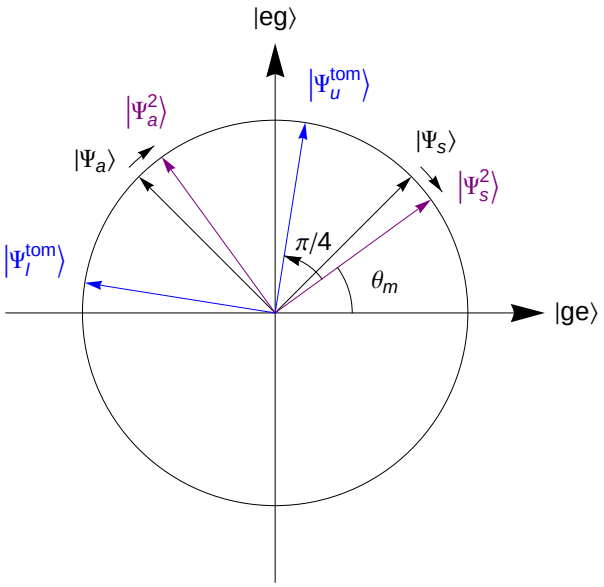

Figure 5.13: Compensation of the not perfect decoupling of the qubits. The prepared states are slightly shifted in order to be symmetric in the basis of the far detuned qubits

(5.33). It corresponds to a mixing angle of 0.45π. The lower state has still a slight contribution from the antisymmetric state $|Psi_\mathrm{a}\rangle$, as discussed in Section 5.4. Or in other words, it is of the form $|\Psi_\mathrm{l}^\mathrm{tom}\rangle = \gamma|ge\rangle - \sqrt{2}\alpha|\Psi_\mathrm{a}\rangle$, where $\alpha = \sin\theta_\mathrm{m}$ is small and $\gamma = \beta - \alpha$. For a prepared symmetric state $|\Psi_\mathrm{s}\rangle$, the diagonal element is then given by $|\langle\Psi_\mathrm{l}^\mathrm{tom}|\Psi_\mathrm{s}\rangle|^2 = |\gamma|^2 = 0.34$. The upper state has a slightly symmetric contribution. Therefore the symmetric state has a bigger overlap with the upper state than with the lower state and $|\langle\Psi_\mathrm{u}^\mathrm{tom}|\Psi_\mathrm{s}\rangle|^2 = 0.66$. For the antisymmetric state $|\Psi_\mathrm{a}\rangle$ a similar argument applies. For the symmetric state, the measured state was therefore not totally symmetric, as seen in Fig.5.12.

To check if the basis change was justified, one can get equal diagonal elements in the tomography basis by shifting the qubit A by -16 MHz. In the single qubit basis $|eg\rangle$ and $|ge\rangle$, the diagonal elements of the density matrix are not equal anymore. This -16 MHz shift corresponds to changing the mixing by an angle of -0.05π. The corresponding sketch can be seen in Fig. 5.13. The generated phase then have a mixing angle difference of $\pi/4$ to the detuned qubits basis. The symmetric state $|\tilde{\Psi}_\mathrm{s}\rangle$ is then not anymore totally symmetric, but has a higher overlap with qubit B, $|ge\rangle$. The corresponding diagonal elements become equal in amplitude $|\langle\Psi_\mathrm{u}^\mathrm{tom}|\tilde{\Psi}_\mathrm{s}\rangle|^2 = |\langle\Psi_\mathrm{l}^\mathrm{tom}|\tilde{\Psi}_\mathrm{s}\rangle|^2 = 0.5$.

This shift was also conducted experimentally. It can be seen as a good hint, that the above considerations are valid: for a detuning of $\Delta_{tom} = 240$ MHz and a shift of qubit A, $\Delta_{gen} = -13 \pm 2$ MHz, during the generation procedure. It can be seen in figure Fig. 5.14. Again the first state is rotated by -0.33π. And the shift of Qubit A is determined in Ramsey measurements, described in Section 5.4. This measurement should be a check, where the asymmetry of the

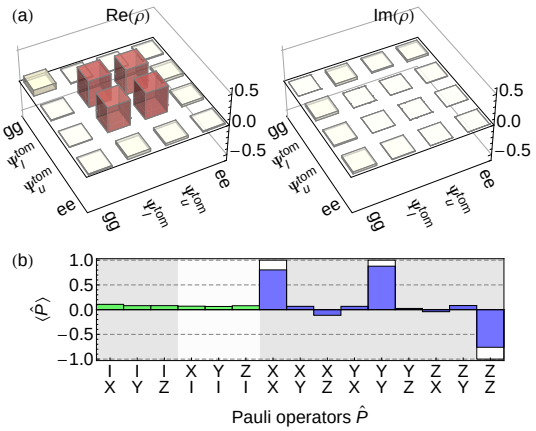

Figure 5.14: Symmetric state in the basis of the dispersive Hamiltonian with 240 MHz detuned qubits and a J-coupling of 25 MHz. The scale is the same as in Fig. 5.11

states in Fig. 5.11 is coming from and there seems to be a good agreement to the theory.

To check it more precisley, it would be better to change the pattern in Fig. 5.10 and to start with far detuned qubits. And then shortly tune them into resonance for the excitation of the symmetric and antisymmetric state. For example leave qubit A and B at their sweet spot and then tune A in resonance with qubit B. But the flatness of the fluxpulse is not anymore totally given. And qubit A will leave the resonance. As well, a strong 70 μs fluxpulse will induce certain heating.

5.7 Bell state generation

The Bell-type states have drawn a lot of attention as they are maximally entangled states. They can be used to violate Bell's inequality [42, 43]. Another field of interest is quantum computation [44, 23].

Here a method is shown how to generate this states in a shorter time sequence than in the previous section. The pulse sequence used is shown in Figure 5.15. First qubit B is excited with a π pulse and then the qubits are tuned into resonance for 14 ns. There is a 5 ns intermediated step at the beginning of the flux pulse in order to reduce the flux pulse overshoot. The excitation is oscillating between the two qubits due to the dispersive $J_{\mathrm{A,B}}$-coupling. After waiting a quarter of a period, the two qubit state is the maximally entangled Bell state, which is then read out with quantum state tomography, see Fig. 5.16. Again the dynamic phase picked up by qubit A during the frequency excursion away from the biasing frequency during the flux pulse is compensated by rotating the phase of qubit A by 0.274π after the reconstruction of the two qubit state.

The length as well as the fluxpulse amplitude was determined by measuring the oscillation of the excited state of qubit B. Coming from the $J_{\mathrm{A,B}}$-coupling of 25MHz, only 5 ns of resonance would be needed to entangle the qubits. Therefore, slight timing errors have a huge impact. and the fidelity was found

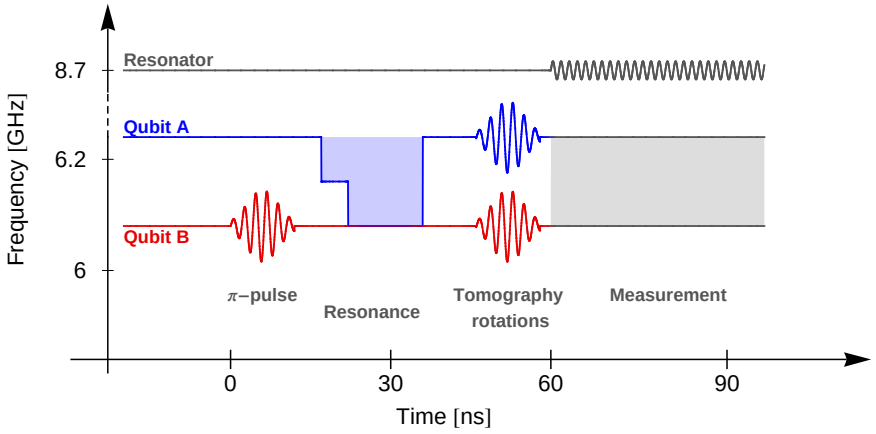

Figure 5.15: Bellstate generation by excitation of one qubit an then swapping the excitation until the excitation is equally distributed. The fluxpulse length was 14ns, not including a 5 ns buffer before the resonance.

to be 93.3%, neglecting the dynamical phase error.

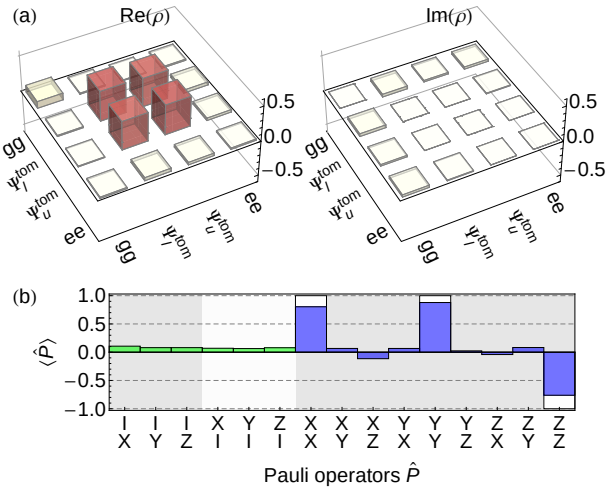

Figure 5.16: Bellstate generated by a short resonant time, using the scheme of Fig. 5.16

.

Chapter 6

Three qubit states

In this chapter, we discuss the collective dispersive coupling between three qubits and the generation of three qubit entanglement. Again the new eigenstates of the system consists of dark states and 3 qubit entangled states. There is the forming of Dicke states. Three qubit entanglement is important for quantum processing is many algorithms, such as the bit flip error correction or for a potential storage states s[45, 46]. First the anticrossing will be investigated in Section 6.1. This will be followed by a discussion of the states of the avoided crossing in Section 6.1. Then Section 6.3 will concern the W state generation.

6.1 Anticrossing of three qubits

The dispersive exchange coupling, discussed in Section 5.3, also leads in the three qubit case to an avoided crossings. The discussion of this anticrossing is important, in order to find the Dicke states. From this anticrossing, one can read out, if the qubits are in resonance or not. The dispersive couplings can also be read of from the avoided crossing with the method from Section 5.4. This points will be discussed in the following paragraphs.

To compare the resonance of three qubits and two qubits, first the dispersive coupling between two qubits is investigated, neglecting the third qubit. In order to do so, two qubits are tuned to 5GHz, while the third is tuned 500 MHz away. 5 GHz is the flux sweet spot of qubit C and the highest frequency point, which is reachable for all qubits. The values found for the dispersive exchange coupling are $J_{\mathrm{A,C}} = 2.5 \pm 1$ MHz, $J_{\mathrm{A,B}} = 16.6 \pm 1.6$ MHz and $J_{\mathrm{B,C}} = 16.4 \pm 0.9$ MHz. The small coupling between qubit A and C has the following reason: They couple directly to each other capacitively over the resonator, as they are spatially very close, see Fig. 3.1. This coupling cancels the coupling over the resonator by virtual photons.

As in the two qubit case, the dispersive $J_{a,a^{\prime}}$-coupling is smaller than the calculated values from formula (5.31). They are roughly one half. The same discussion applies as for the coupling at 6 GHz, which can be found in Section 5.4. The different amplitudes for $J_{\mathrm{A,B}}$ at 5 GHz and 6 GHz can be explained by the different detunings from the resonator and by the square root dependence of the coupling strength g on the qubit frequency. The calculated value from $J_{\mathrm{A,B}}^{6\mathrm{GHz}}$ for $J_{\mathrm{A,B}}^{5\mathrm{GHz}}$ is 16(.2) MHz.

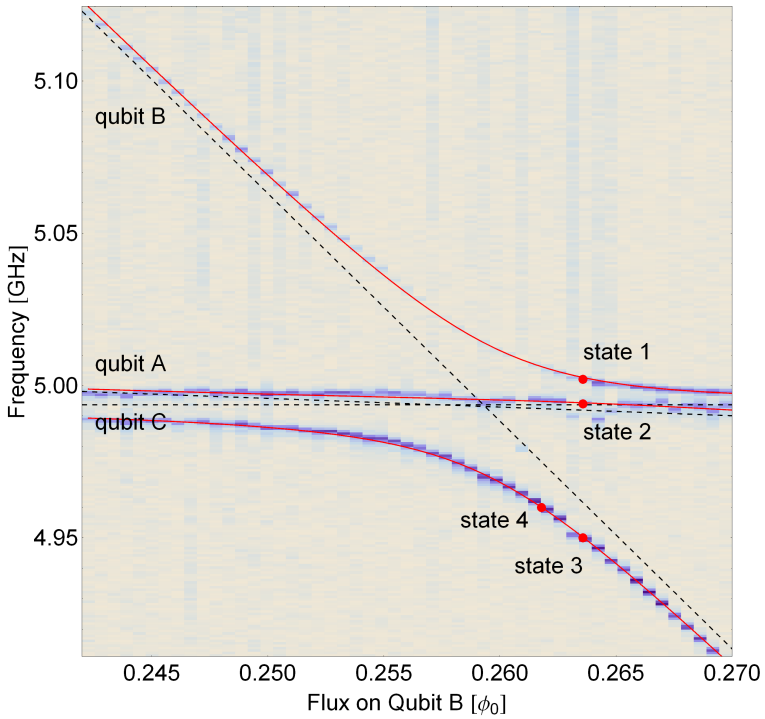

Figure 6.1: Anticrossing of three qubits: Qubit B is tuned through the resonance of qubit A and C. The red lines shows a fit to the energy levels from diagonalizing the three qubit dispersive Hamiltonian. The black doted line corresponds to single qubit frequencies. Qubit C is constraint to be constant. The states 1-4 of the anticrossing are discussed in Section 6.2

.

To get three qubits into resonance, first qubit A and C are brought into resonance and then qubit B is tuned through this resonance, seen in Fig. 6.1. Like in the two qubit case, again the energies were fitted to find the dispersive exchange coupling and the qubit frequency. The following procedure was applied: According to formula (5.30), there are three states in the first excitation manifold, beside the resonator state. The excitation manifolds are not mixed, as the dispersive exchange coupling doesn't change the number of excitations. Therefore one has to diagonalize a 3x3 matrix to find the energies. The effective, reduced Hamiltonian simply reads

$$H_{red} = \begin{pmatrix} \omega_{\mathrm{A}}^{\mathrm{ge}} & J_{\mathrm{A,B}} & J_{\mathrm{A,C}} \\ J_{\mathrm{A,B}} & \omega_{\mathrm{B}}^{\mathrm{ge}} & J_{\mathrm{B,C}} \\ J_{\mathrm{A,C}} & J_{\mathrm{B,C}} & \omega_{\mathrm{C}}^{\mathrm{ge}}. \end{pmatrix} \tag{6.1}$$

The energies of the subsystem are found by using the trigonometric cubic formula[47]. In contrast to other root functions, for example Cardano's method, they are real and ordered in magnitude[48].

The dispersive coupling strengths extracted from the fit to the data shown in Fig. 6.1 are $J_{\mathrm{A,B}} = 12.5 \pm 1.5$ MHz, $J_{\mathrm{B,C}} = 17.4 \pm 1$ MHz and $J_{\mathrm{A,C}} = -2.3 \pm 0.3$ MHz. The different signs are coming from the different positions of the qubits in the cavity, which can be seen in Figure 3.1 and 5.6 and from Equation (5.31). To find out, where the difference to the two qubit measured values is coming from, one can constrain the fit on the individually measured values. The residual, or the root mean square of the errors, is then only changing by 0.5%. So the fit to this data is not really sensitive to small perturbations in the dispersive exchange coupling strength.

However the small difference might also come from qubit A. It is operated 0.302 Φ_0 from the magnetic flux sweet spot, which makes it sensitive to flux noise. Drifts and jumps up to 10 MHz were observed within 30 minutes. This could explain the drift of qubit A in Fig. 6.1, as the shown measurement took two hours. On the other hand, the collective system, when all qubits are roughly in resonance, was observed to drift only 3 MHz in 10 hours. Obviously, the effect of the qubit A drift is screened in this measurement of the collective system, has the qubit A drift affects more than one state. Another reason is the following: From the crosstalk of the flux lines, one would expect Qubit A to change $4.6\,10^{-4}$ Φ_0 or 5.5 MHz over the whole pattern. Which is less than extracted from the fit: 9 MHz. On the other hand, taking qubit A to be constant in the fit changes the root mean square error by 20%.

6.2 3 Qubit Dicke state

In analogy to the measurements discussed in Section 5.6, one can also measure the symmetry of 3 qubit states. One can have a look if the anticrossing states are really Dicke states or not. First one has to note, that due to different coupling strengths, tuning all qubits just in resonance, doesn't produce symmetric states. We have decided to investigate the W state, as it is a very important state for many quantum information algorithms and it shows three-qubit entanglement [45, 46].

In the following, a scheme to find the W state, defined by $|W\rangle = 1/\sqrt{3}(|egg\rangle + |geg\rangle + |gge\rangle)$ is presented. However, the state found by applying the scheme is

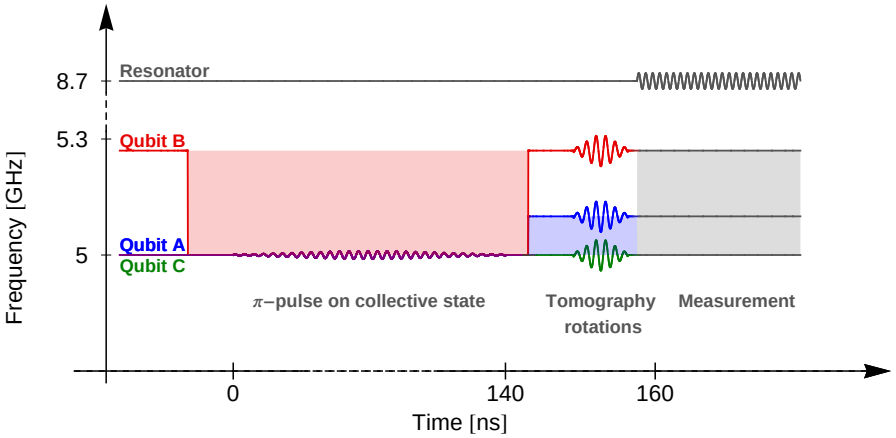

Figure 6.2: Pulse scheme for the generation and tomographic reconstruction of three qubit Dicke states: Qubit B, which couples the most to the other qubits is tuned to qubit A and C with a flux pulses. The relevant Dicke state is then prepared by applying a microwave pulse simultaneously to all three qubits with a fixed phase and amplitude relation. After the preparation, qubit A and C are detuned by 100MHz and qubit B is brought to its initial position in order to apply quantum state tomography.

not the W state. Nevertheless, the state is shown, in order to investigate, where the error is coming from. It is not obvious and different mechanism come into consideration, why the wrong state was generated. There is no final conclusion, why this error is there. The main part of this section is dedicated to the search of the error source. For completeness, the other two states at the given qubit detuning are shown as well. Nevertheless the W state was found and is presented at the end of the section.

First we have look how we prepare and readout the anticrossing states. The pulse scheme used is shown in Fig. 6.2. The state is driven with a weak Gaussian pulse, as the detuning to the next one-excitation state is normally very small, and two photon transitions are lying between. After this pulse, the qubits are detuned in order to perform quantum state tomography and read out the qubits.

For generating a symmetric W-state, we leave qubit B slightly detuned from qubit A and C during the π-pulse, instead of tuning all qubits in resonance. This is due to the different dispersive couplings. The detuning between the qubits should be

$$\begin{aligned} \omega_{\mathrm{B}}^{\mathrm{ge}} - \omega_{\mathrm{A}}^{\mathrm{ge}} &= J_{\mathrm{A,C}} - J_{\mathrm{A,B}} \\ \omega_{\mathrm{A}}^{\mathrm{ge}} - \omega_{\mathrm{C}}^{\mathrm{ge}} &= J_{\mathrm{B,C}} - J_{\mathrm{A,B}}, \end{aligned} \tag{6.2}$$

to get a W-State. This can easily be seen from Equation (6.1) by calculating the energy of a W state. The eigenstates, ordered in energy, for $J_{\mathrm{A,B}} = J_{\mathrm{B,C}} = 16$ MHz and $J_{\mathrm{A,C}} = -2.5$ MHz are $|W\rangle$, $1/\sqrt{2}\,(|egg\rangle - |gge\rangle)$ and $1/\sqrt{6}\,(|egg\rangle - 2|geg\rangle + |gge\rangle)$.

The measured density matrix and Pauli sets of the first state, created following this scheme, is shown in Fig. 6.3. Only the real part is shown, as the

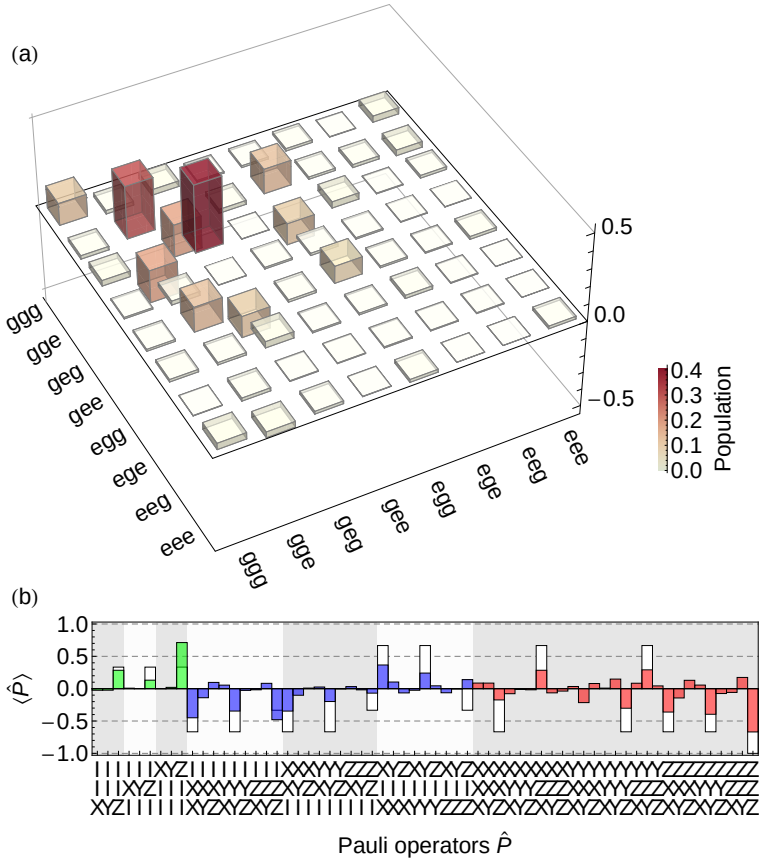

Figure 6.3: State 1: Anticrossing state of the highest energy band in Fig. 6.1 near the expected W state. a) Real part of the density matrix with a dominant term of qubit B. b) corresponding Pauli set.

imaginary part is roughly zero. There is quiet a big decay during the generation of the state, which give the corresponding $|ggg\rangle$ population. The the signs of the off-diagonal elements are not the same, which would be needed for a symmetric W-state. The asymmetry of the diagonal elements of the first excitation manifold (egg, geg, gge) is obvious and the state is not the expected $|W\rangle$-state.

One error source for this is the state tomography itself: the ground state was reconstructed with a fidelity of 92%, which is rather low[22]. Nevertheless this measurement of the presumed W-state was repeated twice from scratch and qualitavely the same assymetry was found. This is remarkable, given large frequency shifts of qubit A, discussed in the previous section and the bad state tomogrpahy. However, this hints to a systematical error.

As in Section 5.6, the finite detuning of the qubits can influence the state tomography. The single eigenstates of the reduced Hamiltonian (6.1) during the read-out procedure, seen in Fig. 6.2, are

$$\begin{aligned} |\Psi_{\bar{A}}^{\mathrm{tom}}\rangle &= (0.995, -0.095, -0.041) \\ |\Psi_{\bar{B}}^{\mathrm{tom}}\rangle &= (0.097, 0.994, 0.060) \\ |\Psi_{\bar{C}}^{\mathrm{tom}}\rangle &= (0.035, -0.063, 0.997), \end{aligned} \tag{6.3}$$

and they still have a not negligible overlap with other bare qubit states. This can still have an impact on the state tomography, as we have seen in Section 5.6. Therefore the states are projected on the single qubit states, which changes the elements of the density matrix by roughly 15%. Hence, it doesn't have the same impact as in the two qubit case. Nevertheless it was done for all density matrices, shown in this chapter.

The main error source for the wrong state might be a simple sign error. As it can be seen in Equation (6.2), the state is highly depending on the sign of the dispersive exchange couplings. The position even alters between the different energy levels of Fig. 6.1, depending on the sign. The sign of $J_{\mathrm{A,B}}$ was investigated in Section 5.6. It is positive, else it would exchange the symmetric and the antisymmetric state at the avoided crossing [28]. Hence, the wrong sign could come from the other two couplings. Another indication to different signs are the off-diagonal elements. They indicate that the state is not a symmetric state, meaning not all amplitudes of the state have the same sign. This indicates that the W state, which is symmetric, is on a different energy level, seen in Fig. 6.1.

In order to investigate the detuning of Qubit A and C, one can have a look at the state next to the previously measured. As expected from diagonalizing the Hamiltonian (5.30), the state 8 MHz next to the previously discussed state is an antisymmetric Bell-state in a 2 qubit subspace, $|\Psi_{Bell}^{-}\rangle = 1/\sqrt{2}(|egg\rangle - |gge\rangle)$. The measured density matrix and Pauli set is shown in Fig. 6.4. This is a good indication, that qubit A and C are really in resonance, as the Bell state is very sensitive to detuning between qubit A and C. This was investigated by numerically diagonalizing the Hamiltonian (5.30). Nevertheless it could also be a reminiscent from the bad tomography and the finite detuning during the tomography and the detuning during the π-pulse. It also indicates that the asymmetry of the diagonal elements in Fig. 6.3 might come from a detuning of qubit B.

To get the whole picture of the situation, one can also determine the symmetry of the third state, seen in figure 6.5. One would expect the $1/\sqrt{6}(|egg\rangle -$

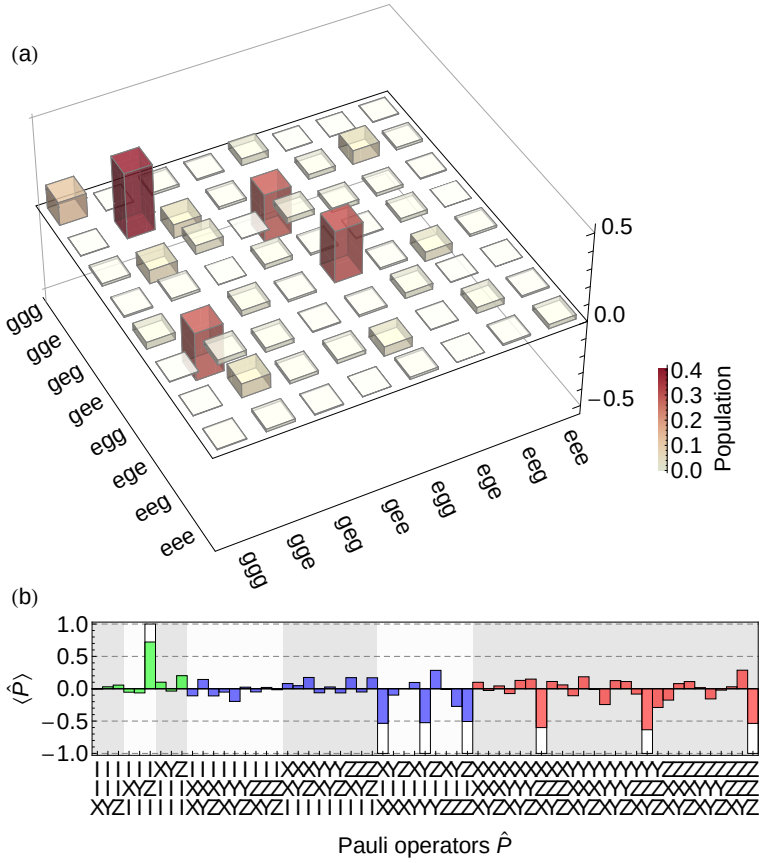

Figure 6.4: State 2: a Bell state a) Real part of the density matrix with a Bell state between Qubit A and C. b) corresponding Pauli set with the theoretical expectation values of the Pauli operators for the antisymmetric Bell state $|\Psi^{-}_{Bell}\rangle$.

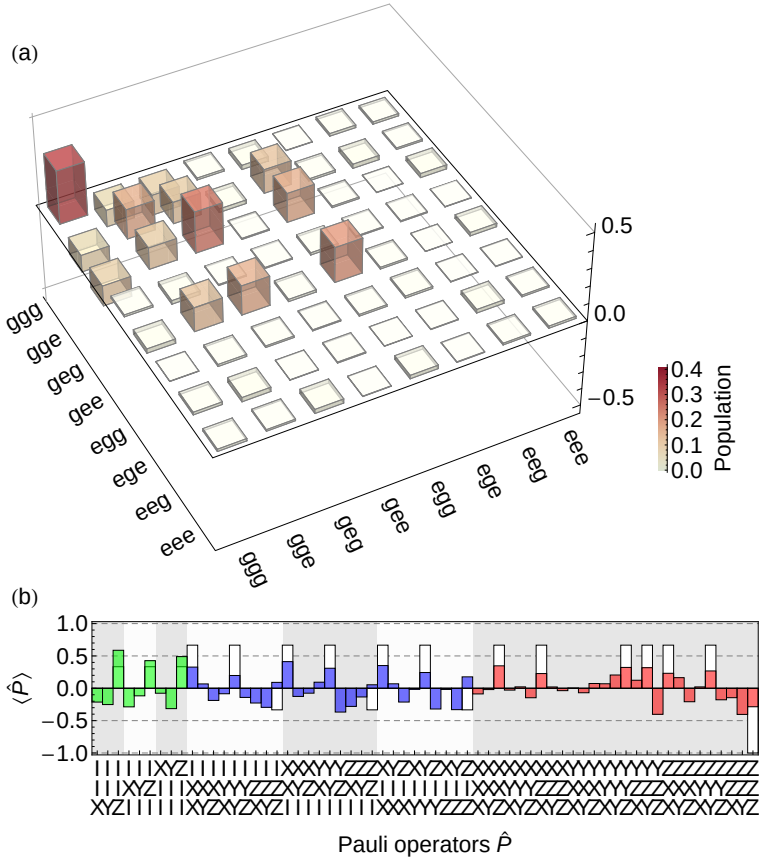

Figure 6.5: State 3 of the lowest energy band a) Real part of the symmetric state with an off resonant drive b) corresponding Pauli set with the theoretical expectation values of the Pauli operators for the W state.

$2|geg\rangle + |gge\rangle$) state. The large off-diagonal elements $|ggg\rangle\langle gge|$,$|ggg\rangle\langle geg|$ and $|ggg\rangle\langle egg|$ are coming from an off-resonant state preparation pulse. Those off-resonant terms also have a large imaginary part, which is not shown, as it only indicates, how the state is driven. The off-diagonal elements $|geg\rangle\langle egg|$,$|gge\rangle\langle egg|$ and $|gge\rangle\langle geg|$ of the first excitation manifold indicate, that all basis states have the same sign. Therefore one can investigate this energy band further to find the W-state.

Shifting the qubit B by 14 MHz to a larger frequency gives the searched W-state with a fidelity of 67%, shown in Figure 6.6, where qubit B was rotated by 0.45π and qubit A by 0.04π during data processing. The state was generated using a 160ns long Gaussian pulse. The fidelity is limited by the decay, which populates the ground state and the decoherence, as mentioned in the text before. The working of this method again indicates that there is a sign error in the dispersive exchange coupling, as the W-state is not on the expected energy level.

To conclude, one can say, that there are many indications to an unknown sign

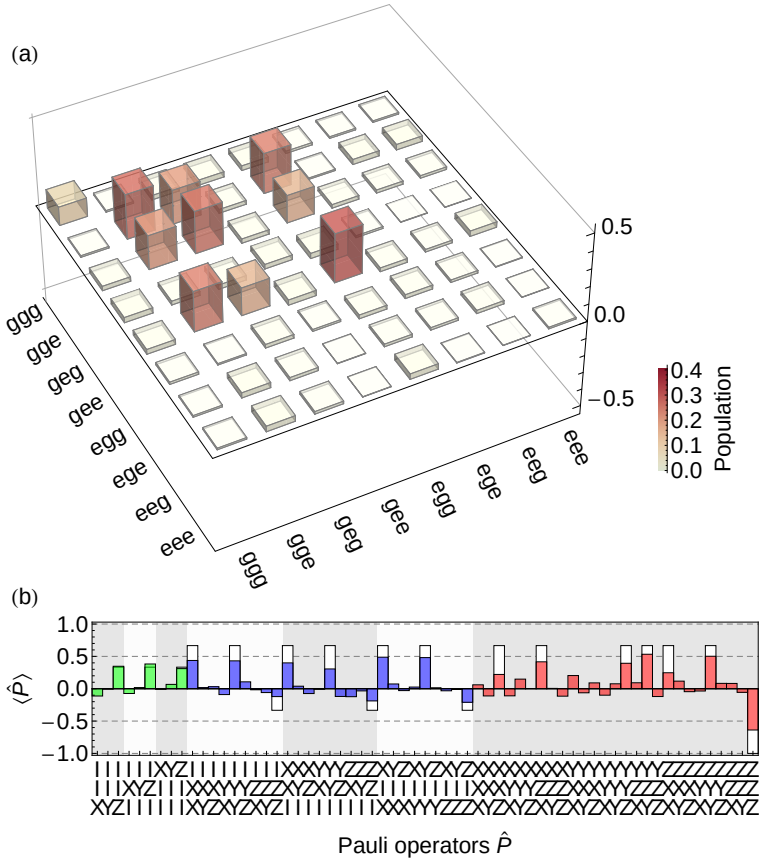

Figure 6.6: State 4, W-state a) Real part of the density matrix, the state decays and has decoherence during the 160ns long Gaussian pulse b) corresponding Pauli set with the theoretical expectation values of the Pauli operators for the W state.

error in the dispersive exchange coupling. And it seems, that single states are addressable, although qubits are shifting. This data should be further analyzed using higher transmon levels, which were neglected during the analysis. Also the approximation of the Jaynes Cummings Hamiltonian in the dispersive regime should be made with higher orders in $g/(\omega_\mathrm{r} - \omega_a)$, leading to other coupling mechanisms than only the dispersive exchange coupling $J_{a,a'}$. On the other hand, also a systematical error in the state tomography could be the reason, which would also affect the result in the next section.

6.3 W-state generation

For quantum information processing, the W-state needs to be generated fast. The W-state can for example be used as a memory state due to its robustness to qubit loss [45]. In analogy to Section 5.7, such a generation scheme is shortly reviewed. And the tripartite entanglement is shown later in the text.

The pattern is nearly the same as in Fig. 6.2, with the difference, that qubit B is first excited and then tuned in resonance with qubit A and C. The excitation then oscillates between the states due to the dispersive exchange coupling. For the state in Fig. 6.7, the resonance time is 7,5 ns long and the produced state is measured with quantum state tomography.

It has a fidelity of 77%. This is on the same order of magnetidue as previously reported experiments in circuit QED:78% [46]. However the presented result has a large error due to the bad state tomography, which could be improved. Also the phase of qubit A was rotated by 0.84π during data processing.

To investigate the entanglement, one can use entanglement witnesses[46, 22]. An entanglement witness is a function which detects entanglement. An operator $\hat{W}$ is an entanglement witness, if $\mathrm{Tr}(\hat{W}\hat{\rho}) \geqslant 0$ for all separable states $\hat{\rho}$ and $\mathrm{Tr}(\hat{W}\hat{\rho}) < 0$ for some entangled states. If $\mathrm{Tr}(\hat{W}\hat{\rho}) < 0$ the entanglement is detected. This is a sufficient condition, but not necessary condition. In general there are many different entanglement witnesses, which detect different entanglement.

In order to detect entanglement, not the full state tomography needs to be done, but only this witness could be measured. Which is very convenient for a large number of qubits. In our case the whole density matrix was measured anyway, and it can be used. A simple entanglement witness is

$$\hat{W}_W = \frac{2}{3} I - |W\rangle\langle W|, \tag{6.4}$$

and $|W\rangle$ is the pure W-state. Hence, the state is tripartite entangled if $\langle W|\hat{\rho}|W\rangle > 2/3$. This is obviously the case for this measurement, as $77\% > 67\%$. So it is trully not a biseparable state.

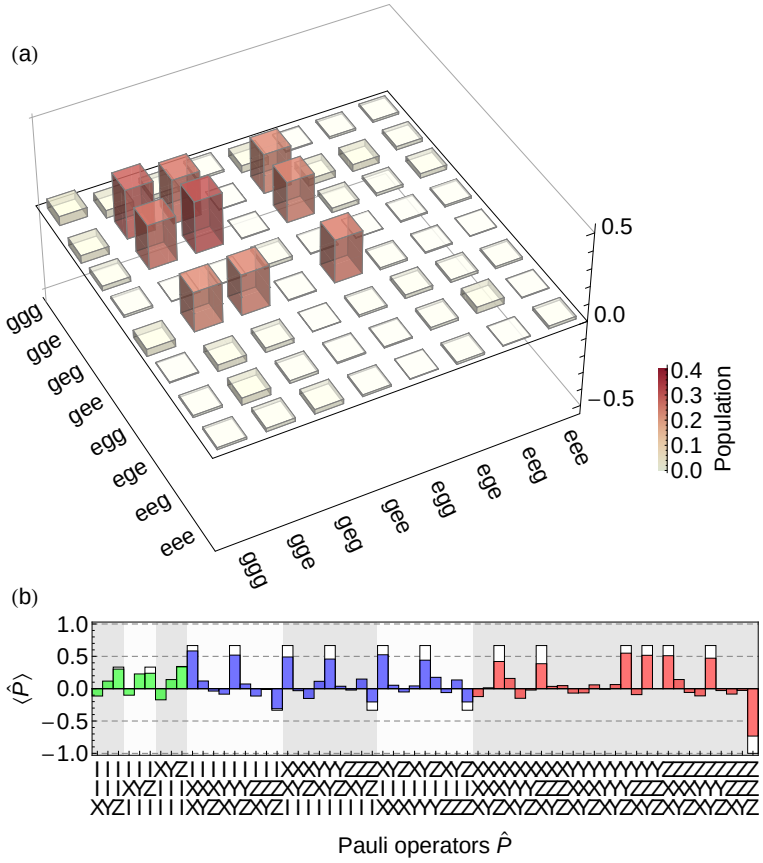

Figure 6.7: W-state produced by oscillating an excitation between the qubits a) Real part of the density matrix, with an higher population of qubit B b) corresponding Pauli set with the theoretical expectation for the W state.

Chapter 7

Conclusion

In this thesis the effect of magnetic flux pulses, the dispersive exchange coupling of two and three qubits, as well as the generation of entanglement between qubits in circuit QED was studied.

For the magnetic flux pulses, many different sources of distortions from the optimal value were identified. For example, the presence of a large inductance was recognized and heating due to flux pulses was observed. The large inductance can be overcome by applying a second flux pulse opposite in amplitude, whereas the heating can be compensated by applying a constant amount of flux pulses for a long time, until the temperature of the sample is stabilized at a slightly higher temperature.

For the second topic discussed in the thesis, the implementation of a two qubit Dicke-like Hamiltonian, where a certain asymmetry of the coupling strengths remains, and the study of the dispersive exchange coupling, good results were achieved. The fully characterized Dicke states are in good agreement with the theoretical prediction. The main challenges were the finite detuning of the qubits during the tomographic process, as well as the not perfect flux pulses. However, the sub-/superradiant character of the states was not observed, as the associated Purcell effect might not have been the preliminary decay channel in our setup. On the other hand symmetry selective Rabi oscillations between these states were found.

In the three qubit case, distinct qubit states of the avoided crossing were fully characterized. Though, a certain mismatch between the theory and the experiment was recognized. It might be accounted to an unknown phase difference between the dispersive exchange couplings or a not perfect quantum state tomography.

The dispersive exchange coupling was also used to entangle the qubits in a few nanoseconds. The results where Bell states as well a W-class-state.

All these studied mechanisms can be used to observe advanced quantum information processing algorithms and even more sophisticated quantum mechanical effects for more than three qubits. In the future, the number of qubits might even be extended to observe the Dicke superradiant phase transition [49, 50]. Or, with an array of resonators coupled to the qubits, it could also be possible to implement a Bose and Jaynes-Cummings Hubbard model [51] and to investigate the superfluid to Mott transition of light [12, 52].

On the other hand, circuit quantum electrodynamics is a promising candi-

date for the implementation of a quantum computer. Nevertheless coherence is still an issue for the scalability to an arbitrary quantum computer, but there are many suggestions [53] how to address this problem. Elaborated algorithms for two [44] and for three [24, 23, 54, 55] qubits have been shown, promising a bright future with good prospects.

Acknowledgments

First of all I want to thank professor Andreas Wallraff for giving me the opportunity to conduct this experiments in his group, in this exciting field of research and for being part of this awesome lab.

Special thanks goes to Matthias Baur, my supervisor. It would have been much harder without his support, effort and expertise during the whole thesis. He was patient with my beginner's questions and spent a lot of time in lab for outstanding guidance. And he thought me how to tackle practical physical problems.

Also Arkady Federov's support needs to be acknowledged. He was a big help with theoretical, as well as with practical issues. Lars Steffen deserves credit for his competence in cryostatic and practical support. I also want to appreciate Stefan Filipp‘s assistance and for sharing his broad insight into physics. Thank goes as well to Tobias Thiele for the fruitful discussions and great help.

Moreover I am grateful to the whole Qudev group, who developed the software and hardware to the current state, which allowed to carry out this work. Especially, there was always a helping hand from Christian Lang, Jonas Mlynek, Arjan van Loo and Abdufarrukh Abdumalikov.

I also want to thank Annette Schuetze for the encouragement and graphical support. Especially her patience with my night shifts needs to be mentioned. Last, but not least, I want to thank my family and friends for supporting me during my whole studies and during my thesis. They were always a really safe harbor.

Bibliography

[1] A. Messiah, *Quantenmechanik 1.* deGruyter, Berlin, 1991.

[2] D. Deutsch, "Quantum theory, the Church-Turing principle and the universal quantum computer," *Proceedings of the Royal Society of London. Series A, Mathematical and Physical Sciences*, vol. 400, pp. 97–117, July 1985.

[3] M. A. Nielsen and I. L. Chuang, *Quantum Computation and Quantum Information.* Cambridge University Press, 2000.

[4] R. L. Rivest, A. Shamir, and L. Adleman, "A method for obtaining digital signatures and public-key cryptosystems," *Commun. ACM*, vol. 21(2), pp. 120–126, 1974.

[5] L. K. Grover, "A fast quantum mechanical algorithm for database search," in *Proceedings of the twenty-eighth annual ACM symposium on Theory of computing*, (Philadelphia, Pennsylvania, United States), pp. 212–219, ACM, 1996.

[6] R. P. Feynman, "Simulating physics with computers," *International Journal of Theoretical Physics*, vol. 21, pp. 467–488, June 1982.

[7] D. I. Schuster, *Circuit Quantum Electrodynamics.* PhD thesis, Yale University, 2007.

[8] D. P. DiVincenzo, "The physical implementation of quantum computation," *Fortschritte der Physik*, vol. 48, no. 9-11, pp. 771–783, 2000.

[9] S. Filipp, P. Maurer, P. J. Leek, M. Baur, R. Bianchetti, J. M. Fink, M. Göppl, L. Steffen, J. M. Gambetta, A. Blais, and A. Wallraff, "Two-qubit state tomography using a joint dispersive readout," *Phys. Rev. Lett.*, vol. 102, no. 20, p. 200402, 2009.

[10] J. Majer, J. M. Chow, J. M. Gambetta, J. Koch, B. R. Johnson, J. A. Schreier, L. Frunzio, D. I. Schuster, A. A. Houck, A. Wallraff, A. Blais, M. H. Devoret, S. M. Girvin, and R. J. Schoelkopf, "Coupling superconducting qubits via a cavity bus," *Nature*, vol. 449, pp. 443–447, Sept. 2007.

[11] M. Göppl, A. Fragner, M. Baur, R. Bianchetti, S. Filipp, J. M. Fink, P. J. Leek, G. Puebla, L. Steffen, and A. Wallraff, "Coplanar waveguide resonators for circuit quantum electrodynamics," *J. Appl. Phys.*, vol. 104, p. 113904, 2008.

[12] J. Fink, *Quantum nonlinearities in strong coupling circuit QED*. PhD thesis, ETH Zurich, 2010.

[13] R. N. Simons, *Coplanar waveguide circuits, components and systems*. Wiley Series in Microwave and Optical Engineerging, Wiley Inter-Science, 2001.

[14] R. Feynman, *Lectures on Physics Vol.2*. Addison-Wesley, Reading, 1964.

[15] M. H. Devoret, A. Wallraff, and J. M. Martinis, "Superconducting qubits: A short review," *cond-mat/0411174*, vol. -, 2004.

[16] A. Cottet, *Implementation of a quantum bit in a superconducting circuit*. PhD thesis, Universite Paris 6, 2002.

[17] I. S. G.Blanch, M.Abramowitz, *Handbook of Mathematical Functions*. United States Department of Commerce, 1972.

[18] J. Koch, T. M. Yu, J. Gambetta, A. A. Houck, D. I. Schuster, J. Majer, A. Blais, M. H. Devoret, S. M. Girvin, and R. J. Schoelkopf, "Charge-insensitive qubit design derived from the Cooper pair box," *Phys. Rev. A*, vol. 76, no. 4, p. 042319, 2007.

[19] M. Pechal, "Geometric phase of a harmonic oscillator in circuit qed," Master's thesis, ETH Zurich, 2011.

[20] R. Bianchetti, S. Filipp, M. Baur, J. M. Fink, M. Göppl, P. J. Leek, L. Steffen, A. Blais, and A. Wallraff, "Dynamics of dispersive single-qubit readout in circuit quantum electrodynamics," *Phys. Rev. A*, vol. 80, no. 4, p. 043840, 2009.

[21] M. D. Reed, L. DiCarlo, B. R. Johnson, L. Sun, D. I. Schuster, L. Frunzio, and R. J. Schoelkopf, "High-fidelity readout in circuit quantum electrodynamics using the jaynes-cummings nonlinearity," *Phys. Rev. Lett.*, vol. 105, p. 173601, Oct 2010.

[22] L. DiCarlo, M. D. Reed, L. Sun, B. R. Johnson, J. M. Chow, J. M. Gambetta, L. Frunzio, S. M. Girvin, M. H. Devoret, and S. R. J., "Preparation and measurement of three-qubit entanglement in a superconducting circuit," *Nature*, vol. 467, pp. 574–578, 2010.

[23] M. Baur, A. Fedorov, L. Steffen, S. Filipp, M. P. da Silva, and A. Wallraff, "Benchmarking a teleportation protocol realized in superconducting circuits," *arXiv:1107.4774*, 2011.

[24] A. Fedorov, L. Steffen, M. Baur, M. P. da Silva, and A. Wallraff, "Implementation of a toffoli gate with superconducting circuits," *Nature*, vol. advance online publication, pp. –, Dec. 2011.

[25] M. W. Johnson, M. H. S. Amin, S. Gildert, T. Lanting, F. Hamze, N. Dickson, R. Harris, A. J. Berkley, J. Johansson, P. Bunyk, E. M. Chapple, C. Enderud, J. P. Hilton, K. Karimi, E. Ladizinsky, N. Ladizinsky, T. Oh, I. Perminov, C. Rich, M. C. Thom, E. Tolkacheva, C. J. S. Truncik, S. Uchaikin, J. Wang, B. Wilson, and G. Rose, "Quantum annealing with manufactured spins," *Nature*, vol. 473, p. 194, May 2011.

[26] M. Hofheinz, E. M. Weig, M. Ansmann, R. C. Bialczak, E. Lucero, M. Neeley, A. D. O'Connell, H. Wang, J. M. Martinis, and A. N. Cleland, "Generation of Fock states in a superconducting quantum circuit," *Nature*, vol. 454, pp. 310–314, July 2008.

[27] S. Sendelbach, D. Hover, A. Kittel, M. Muck, J. M. Martinis, and R. McDermott, "Magnetism in squids at millikelvin temperatures," *Phys. Rev. Lett.*, vol. 100, pp. 227006–4, June 2008.

[28] S. Filipp, A. F. van Loo, M. Baur, L. Steffen, and A. Wallraff, "Preparation of subradiant states using local qubit control in circuit QED." arXiv:1107.2078v1, 2011.

[29] R. H. Dicke, "Coherence in spontaneous radiation processes," *Phys. Rev.*, vol. 93, pp. 99–, Jan. 1954.

[30] M. Gross and S. Haroche, "Superradiance: An essay on the theory of collective spontaneous emission," *Phys. Rep.*, vol. 93, no. 5, pp. 301 – 396, 1982.

[31] Y. Yamamoto and A. Imamoğlu, *Mesoscopic Quantum Optics*. Wiley, 1999.

[32] L. Mandel and E. Wolf, *Optical Coherence and Quantum Optics*. Cambridge University Press, 1995.

[33] E. M. Purcell, "Spontaneous emission probabilties at radio frequencies," *Phys. Rev.*, vol. 69, p. 681, 1946.

[34] S. Filipp, M. Göppl, J. M. Fink, M. Baur, R. Bianchetti, L. Steffen, and A. Wallraff, "Multimode mediated qubit-qubit coupling and dark-state symmetries in circuit quantum electrodynamics," *Phys. Rev. A*, vol. 83, p. 063827, Jun 2011.

[35] A. Blais, J. Gambetta, A. Wallraff, D. I. Schuster, S. M. Girvin, M. H. Devoret, and R. J. Schoelkopf, "Quantum-information processing with circuit quantum electrodynamics," *Phys. Rev. A*, vol. 75, p. 032329, Mar. 2007.

[36] R. Koch, D. DiVincenzo, and J. Clarke, "Model for l/f flux noise in squids and qubits," *Phys. Rev. Lett.*, vol. 98, p. 267003, 2007.

[37] D. F. V. James, P. G. Kwiat, W. J. Munro, and A. G. White, "Measurement of qubits," *Phys. Rev. A*, vol. 64, p. 052312, 2001.

[38] J. A. Smolin, J. M. Gambetta, and G. Smith, "Maximum likelihood, minimum effort," *arXiv:1106.5458*, June 2011.

[39] M. Christandl and R. Renner, "Reliable quantum state tomography," 2011.

[40] F. Motzoi, J. M. Gambetta, P. Rebentrost, and F. K. Wilhelm, "Simple pulses for elimination of leakage in weakly nonlinear qubits," *Phys. Rev. Lett.*, vol. 103, no. 11, p. 110501, 2009.

[41] I. L. Chuang and M. A. Nielsen, "Prescription for experimental determination of the dynamics of a quantum black box," *J. Mod. Opt.*, vol. 44, no. 11, pp. 2455–2467, 1997.

[42] M. Ansmann, H. Wang, R. C. Bialczak, M. Hofheinz, E. Lucero, M. Neeley, A. D. O'Connell, D. Sank, M. Weides, J. Wenner, A. N. Cleland, and J. M. Martinis, "Violation of Bell's inequality in Josephson phase qubits," *Nature*, vol. 461, pp. 504–506, Sept. 2009.

[43] J. S. Bell, "On the Einstein Podolsky Rosen paradox," *Physics (N. Y.)*, vol. 1, p. 195, 1964.

[44] L. DiCarlo, J. M. Chow, J. M. Gambetta, L. S. Bishop, B. R. Johnson, D. I. Schuster, J. Majer, A. Blais, L. Frunzio, S. M. Girvin, and R. J. Schoelkopf, "Demonstration of two-qubit algorithms with a superconducting quantum processor," *Nature*, vol. 460, pp. 240–244, July 2009.

[45] M. Fleischhauer and M. D. Lukin, "Quantum memory for photons: Dark-state polaritons," *Phys. Lett. A*, vol. 65, p. 022314, 2002.

[46] M. Neeley, R. C. Bialczak, M. Lenander, E. Lucero, M. Mariantoni, A. D. O'Connell, D. Sank, H. Wang, M. Weides, J. Wenner, Y. Yin, T. Yamamoto, A. N. Cleland, and J. M. Martinis, "Generation of three-qubit entangled states using superconducting phase qubits," *Nature*, vol. 467, pp. 570–573, 2010.

[47] R. W. D. Nickalls, "Viete, descartes and the cubic equation," *Mathematical Gazette*, vol. 90, pp. 203–208, 2006.

[48] N. Jacobson, *Basic Algebra*. Dover, 2009.

[49] J. Bourassa, J. M. Gambetta, J. A. A. Abdumalikov, O. Astafiev, Y. Nakamura, and A. Blais, "Ultrastrong coupling regime of cavity qed with phase-biased flux qubits," *Physical Review A (Atomic, Molecular, and Optical Physics)*, vol. 80, no. 3, p. 032109, 2009.

[50] P. Nataf and C. Ciuti, "No-go theorem for superradiant quantum phase transitions in cavity qed and counter-example in circuit qed," *Nat Commun*, vol. 1, pp. 72–, Sept. 2010.

[51] S. Schmidt and G. Blatter, "Strong coupling theory for the jaynes-cummings-hubbard model," *Phys. Rev. Lett.*, vol. 103, p. 086403, Aug 2009.

[52] J. Koch and K. Le Hur, "Superfluid-mott-insulator transition of light in the jaynes-cummings lattice," *Phys. Rev. A*, vol. 80, pp. 023811–, Aug. 2009.

[53] M. D. Reed, B. R. Johnson, A. A. Houck, L. DiCarlo, J. M. Chow, D. I. Schuster, L. Frunzio, and R. J. Schoelkopf, "Fast reset and suppressing spontaneous emission of a superconducting qubit," *Appl. Phys. Lett.*, vol. 96, no. 20, p. 203110, 2010.

[54] M. Mariantoni, H. Wang, T. Yamamoto, M. Neeley, R. C. Bialczak, Y. Chen, M. Lenander, E. Lucero, A. D. OConnell, D. Sank, M. Weides, J. Wenner, Y. Yin, J. Zhao, A. N. Korotkov, A. N. Cleland, and J. M. Martinis, "Implementing the quantum von neumann architecture with superconducting circuits," *Science*, vol. 334, no. 6052, pp. 61–65, 2011.

[55] M. D. Reed, L. DiCarlo, S. E. Nigg, L. Sun, L. Frunzio, S. M. Girvin, and R. J. Schoelkopf, "Realization of Three-Qubit quantum error correction with superconducting circuits," *arXiv:1109.4948*, Sept. 2011.